이학박사 학위논문

Supracolloidal chains of diblock copolymer micelles as nanoscale analogues of conventional polymers

고분자의 나노 크기 유사체로서의 이중블록 공중합체 마이셀 초콜로이드 사슬

2023년 2월

서울대학교 대학원
화학부 고분자화학 전공
이 경 현

Supracolloidal chains of diblock copolymer micelles as nanoscale analogues of conventional polymers

지도 교수 손 병 혁

이 논문을 이학박사 학위논문으로 제출함
2023년 2월

서울대학교 대학원
화학부 고분자화학 전공
이 경 현

이경현의 이학박사 학위논문을 인준함
2023년 2월

위 원 장 _____ 이 연 _____ (인)

부위원장 _____ 손 병 혁 _____ (인)

위 원 _____ 정 택 동 _____ (인)

위 원 _____ 김 경 택 _____ (인)

위 원 _____ 유 성 일 _____ (인)

Abstract

Supracolloidal chains of diblock copolymer micelles as nanoscale analogues of conventional polymers

Kyunghyeon Lee
Department of Chemistry
The Graduate School
Seoul National University

Colloidal particles in nanoscale or microscale assemble into well-ordered superstructures such as crystals, chains, and clusters through the interaction between the particles. Superstructures of colloidal particles are promising candidates for new nanomaterials owing to complicated structures and collective properties, which are rarely observed in individual particles. In particular, colloidal particles can assemble into linear supracolloidal chains through bidirectional attraction with orthogonal repulsion. For example, magnetic and electrostatic particles polymerize into supracolloidal chains by using the end-to-end attraction between dipoles with steric repulsion of ligands preventing lateral aggregation. Supracolloidal chains exhibit

cooperative and structural properties for practical applications, which are distinct from constituent particles. For instance, supracolloidal chains of metallic nanoparticles can exhibit plasmon and magnetic coupling through synergetic interaction between particles, which are applicable for sensors and magnetic storage. In addition, periodic and linear nature enables optical and mechanical applications such as one-dimensional photonic crystals, rheological fluids, and colloidal motors.

Chemically and physically distinctive patches on the surface of particles can effectively mediate linear assembly for supracolloidal chains. Each particle requires two patches for the bidirectional attraction, which provide attractive forces via a variety of chemistry such as hydrogen bonding, host-guest interaction, and solvophobic interactions. Especially, block copolymer micelles can assemble into supracolloidal chains by merging of patches induced by segregation of the corona.

Supracolloidal chains can be considered as colloidal analogues of conventional polymers. In this perspective, behaviors of supracolloidal chains have been explained with the assistance of traditional theories of polymers. For example, assembling mechanism of supracolloidal chains can be described using the theory of polymerization including step-growth and chain-growth polymerization. Furthermore, physical dimensions of supracolloidal chains can be measured in the size parameters of polymers such as the contour length, end-to-end distance, and radius of gyration. Using

these parameters, flexibility and conformation of the chains can be suitably explained by the theoretical models of polymer chains such as freely jointed and worm-like chain model. Furthermore, processing and functionalization strategy of polymers can provide inspirations for applications of supracolloidal chains.

This dissertation demonstrates supracolloidal chains of diblock copolymer micelles of PS-*b*-P4VP as nanoscale analogues of conventional polymers. For the assembly of supracolloidal chains, spherical micelles of PS-*b*-P4VP are first converted into patchy micelles. Then, the patchy micelles, the colloidal monomers, polymerize into supracolloidal chains by merging patches in a polar environment. The main purpose of this research is to describe assembling process and flexibility of the supracolloidal chains from the theory of polymers, and find their potential applications by processing and functionalizing the chains. Assembling mechanism of supracolloidal chains is first discussed in Chapter 2. Polymerization of patchy micelles follows the mechanism of step-growth polymerization, where degree of polymerization linearly increases and polydispersity index approaches to two. According to the conventional step-growth equation, a high degree of polymerization is achieved after a certain polymerization time by increasing the initial concentration of patchy micelles. Furthermore, cyclic supracolloidal chains are produced in a very low concentration. The colloidal polymerization is accelerated by adding more water to the solution and employing patchy

micelles having large patches. Flexibility and conformation of supracolloidal chains are elucidated in Chapter 3. By evaluating persistence length, the supracolloidal chains are assessed as semi-flexible, and their conformation is explained by the worm-like chain model of conventional polymers. A self-supporting film of the chains with microscopic pores is produced by spin-coating semi-flexible chains on a solid substrate. PS-*b*-P4VP micelles incorporating CoNPs are demonstrated as colloidal monomers of supracolloidal chains in Chapter 4. By encapsulating cobalt nanoparticles with PS-*b*-P4VP, spherical micelles consisting of cobalt nanoparticles−P4VP shell−PS corona are obtained. Then, the spherical micelles transform into patchy micelles via segregation of PS corona, after crosslinking P4VP shells. Finally, the patchy micelles polymerize into supracolloidal chains by adding water. In this process, undesirable aggregation is prevented by treating P4VP shells with CH_3I, which provides additional repulsive forces.

Keyword: Block copolymer micelle, Self-assembly, Supracolloidal chain, Step-growth polymerization, Semi-flexible chain, Worm-like chain model, Self-supporting film, Cobalt nanoparticle.

Student Number: 2017-29824.

Table of Contents

Abstract ..... **i**

Table of Contents ..... **v**

List of Figures ..... **vii**

Chapter 1. Introduction **1**

1.1. Study Background **2**

1.1.1. Superstructures of colloidal particles 2

1.1.2. Supracolloidal chains from linear assembly of colloidal particles ... 4

1.1.3. Property and application of supracolloidal chains 8

1.1.4. Supracolloidal chains of block copolymer micelles 11

1.1.5. Supracolloidal chains as nanoscale analogues of conventional polymers 14

1.2. Purpose of Research **17**

1.2.1. Motivation 17

1.2.2. Aim and objectives 17

Chapter 2. Step-growth polymerization of patchy micelles of diblock copolymers **25**

2.1. Introduction **26**

2.2. Experimental Section **27**

2.3. Results and Discussion **32**

2.4. Conclusion **38**

Chapter 3. Porous self-supporting film of semi-flexible supracolloidal chains of diblock copolymer micelles **53**

3.1. Introduction **54**

3.2. Experimental Section **55**

3.3. Results and discussion **58**

3.4. Conclusions **64**

Chapter 4. PS-*b*-P4VP micelles incorporating cobalt nanoparticles as building blocks for supracolloidal chains **73**

4.1. Introduction **74**

4.2. Experimental Section **75**

4.3. Results and Discussion **78**

4.4. Conclusion **83**

Bibliography **91**

국문 초록 **109**

List of Figures

Chapter 1. Introduction

Figure 1.1 Superstructures of colloidal particles: (a) colloidal crystal [47]; (b) two-dimensional colloidal superlattice [59]; (c) colloidal cluster [65]. 20

Figure 1.2 Supracolloidal chains from linear assembly of colloidal particles: (a) Magnetic dipolar interaction [75]; (b) Electrostatic dipolar assembly [95]; (c) Hydrogen bonding between patches [109]; (d) Solvophobic interaction between patches [118].....21

Figure 1.3 Properties of supracolloidal chains: (a) plasmonic coupling [128]; (b) magnetic coupling [80]; (c) one-dimensional photonic crystal [143]; (d) micromotor [134].22

Figure 1.4 Self-assembled nanostructures of block copolymers: (a) bulk assembly [160]; (b) solution assembly [164].....23

Figure 1.5 Supracolloidal chains of patchy micelles of block copolymers: (a) poly(ethyleneoxide)-*b*-polystyrene -*b*-poly(2-vinylpydine) [167]; (b) polystyrene-*b*-poly(4-vinylpyridine) [168]; (c) poly(γ-benzyl-L-glutamate)-*g*-poly(ethylene glycol) [171].....24

Chapter 2. Step-growth polymerization of patchy micelles of diblock copolymers

Figure 2.1 Schematic illustration of linear assembly of supracolloidal chains of PS-*b*-P4VP micelles 40

Figure 2.2 TEM images of spherical micelles of PS(51)-*b*-P4VP(18): (a) after staining P4VP with I_2; (b) after staining PS with RuO_4. The scale bars are 100 nm. Schematic illustration of a spherical micelle is depicted in the inset of (a). 41

Figure 2.3 Patchy micelles (top row) and supracolloidal chains (bottom row) of PS(51)-*b*-P4VP(18): (a) and (d) TEM image after staining P4VP with I_2; (b) and (e) TEM image after staining PS with RuO_4; (c) and (f) SEM image. The scale bars are 100 nm. Schematic illustration of a patchy micelle is depicted in the inset of (a).....42

Figure 2.4 Distributions of degree of polymerization *x* of supracolloidal chains after polymerization: (a) 0.5 h; (b) 2 h; (c) 3 h; (d) 6 h. The corresponding SEM images are placed on the right with the scale bar of 500 nm. The green lines are the most-probable distributions, from which the extent-of-reaction values for 0.5 h, 2 h, 3 h, and 6 h are extracted as 0.50, 0.82, 0.86, and 0.93, respectively. 43

Figure 2.5 Evolution of $\bar{x}_n$ and PDI during polymerization: (a) $\bar{x}_n$; (b) PDI. The dotted lines in (a) and (b) are calculated by the conventional step-growth equations of $\bar{x}_n$=1+$2k$[A]$_0t$ and PDI=2−1/$\bar{x}_n$, respectively. The error bars indicate the standard deviations of counting. 44

Figure 2.6 Distributions of degree of polymerization x of supracolloidal chains after 6 h by varying the initial concentration: (a) 1.25 × 10^{-2} wt%; (b) 2.50 × 10^{-2} wt%; (c) 3.75 × 10^{-2} wt%; (d) 5.00 × 10^{-2} wt%. The corresponding SEM images are placed on the right with the scale bar of 500 nm. The green lines are the most-probable distributions. 45

Figure 2.7 Polymerization of supracolloidal chains by varying the initial concentration: (a) $\bar{x}_n$ vs. time; (b) d$\bar{x}_n$/dt vs. [A]$_0$. The dotted lines in (a) are calculated by $\bar{x}_n$=1+$2k$[A]$_0t$. The error bars in (a) indicate the standard deviations of counting. 46

Figure 2.8 TEM image of cyclic supracolloidal chains after staining with I_2. The scale bar is 500 nm. The inset is an enlarged image of a representative cyclic chain in 600 nm × 600 nm. Schematic illustration of the cyclic chain is given at

the left of the inset. 47

Figure 2.9 Effect of the content of water on polymerization of patchy micelles: (a) SEM images after 3h polymerization with the scale bar of 500 nm; (b) $\bar{x}_n$ vs. time. The dotted lines in (c) are calculated by $\bar{x}_n$=1+$2k$[A]$_0t$. The error bars in (c) indicate the standard deviations of counting. Schematic illustration is given above the images.....48

Figure 2.10 GPC results of PS-*b*-P4VP used for assembly of supracolloidal chains. 49

Figure 2.11 TEM images of spherical micelles: (a) PS(25)-*b*-P4VP(7); (b) PS(145)-*b*-P4VP(40). TEM images were obtained after stained with I_2. The scale bars are 100 nm. 50

Figure 2.12 Colloidal polymerization of PS(25)-*b*-P4VP(7) (top row) and PS(145)-*b*-P4VP(40) (bottom row): (a) and (c) TEM images of patchy micelles after staining with RuO_4; (b) and (d) SEM images of supracolloidal chains. The scale bars are 100 nm. 51

Figure 2.13 Evolution of $\bar{x}_n$ for patchy micelles with different size of patches: (a) PS(25)-*b*-P4VP(7); (b) PS(145)-*b*-P4VP(40). The dotted lines are calculated by $\bar{x}_n$=1+$2k$[A]$_0t$. Error bars indicate standard deviations of

counting. Schematic illustrations are given above the corresponding graphs of $\bar{x}_n$ vs. time. 52

Chapter 3. Porous self-supporting film of semi-flexible supracolloidal chains of diblock copolymer micelles

Figure 3.1 TEM images of PS(51)-*b*-P4VP(18) micelles after staining with I_2: (a) spherical micelles; (b) patchy micelles. The scale bars are 100 nm. The inset in (a) and (b) shows an enlarged image (100 nm × 100 nm) of individual spherical and patchy micelles, where the PS corona was stained with RuO_4, respectively. 65

Figure 3.2 Supracolloidal chains of PS(51)-*b*-P4VP(18): (a) SEM image; (b) TEM image after staining the PS corona with RuO_4; (c) TEM image after staining the P4VP core with I_2. All scale bars in images are 100 nm. 66

Figure 3.3 SEM image of supracolloidal chains spin-coated on a substrate. The scale bar is 500 nm.....67

Figure 3.4 Size distributions of supracolloidal chains: (a) contour length; (b) degree of polymerization. The dotted line in (b) corresponds to a most-probable distribution in step-growth polymerization. 68

Figure 3.5 Semi-flexible supracollodial chains: (a) R_g vs. L; (b) R_e vs. L. The dashed lines in (a) and (b) are calculated by Equations 3.2 and 3.3 of the worm-like chain model, respectively.....69

Figure 3.6 SEM images of supracolloidal chains marked with solid circles in Figure 3.5. They are displayed in order of contour lengths. The scale bar is 250 nm. 70

Figure 3.7 SEM images of supracolloidal chains on a substrate after repetitive spin-coating: (a) 5 cycles; (b) 20 cycles; (c) 50 cycles. The scale bars are 500 nm. The bottom inset in (a) is a side-view image in 500 nm × 400 nm, where chains are painted with false colors.....71

Figure 3.8 SEM images of supracolloidal chains on a substrate after repetitive spin-coating: (a) 100 cycles; (b) 200 cycles. The scale bars are 500 nm. The digitized images in (c) and (d) show black spots which are not covered by the chains from the high-resolution images corresponding to (a) and (b), respectively. The bottom inset in (b) shows a photograph of the film (indicated by the arrow) transferred onto a silicon wafer.....72

Chapter 4. PS-*b*-P4VP micelles incorporating cobalt nanoparticles as building blocks for supracolloidal chains

Figure 4.1 Schematic illustration of linear assembly of supracolloidal chains by using PS-*b*-P4VP micelles incorporating CoNPs as colloidal monomers. 84

Figure 4.2 Cobalt nanoparticles (CoNPs): (a) TEM image; (b) Histogram showing the diameters of CoNPs. The scale bar is 50 nm. 85

Figure 4.3 Spherical micelles of PS-*b*-P4VP incorporating CoNPs: (a) TEM image; (b) Histogram of the number of CoNPs in a micelle. The scale bar is 200 nm. The bottom insets show enlarged TEM images of spherical micelles in 100 × 100 nm. The TEM image in the right inset is obtained after staining PS with RuO_4. Schematic illustration is depicted in the upper inset.....86

Figure 4.4 Patchy micelles of PS-*b*-P4VP incorporating CoNPs: (a) TEM images; (b) TEM images after staining with RuO_4; (c) Histogram of the number of patches. The scale bars are 100 nm. The insets show enlarged TEM images of patchy micelles in 100 × 100 nm. Schematic illustration is depicted in the inset of (a). 87

Figure 4.5 TEM image of supracolloidal chains of PS-*b*-P4VP

incorporating cobalt nanoparticles. The scale bar is 200 nm. 88

Figure 4.6 TEM images of CoNPs and micelles incorporating CoNPs after dried in the presence of a magnetic field: (a) CoNPs; (b) spherical micelles; (c) patchy micelles. The scale bars are 1 μm. The inset in (c) shows the magnified image in 500 nm × 400 nm. 89

Figure 4.7 TEM image of supracolloidal chains incorporating CoNPs after dried in the presence of a magnetic field. The scale bar is 2 μm. 90

Chapter 1. Introduction

1.1. Study Background

1.1.1. Superstructures of colloidal particles

Colloidal particles

Colloidal particles in nanoscale or microscale have been widely studied as fundamental elements of nanoscience. There is a huge library of colloidal particles with various sizes, shapes, and compositions, which are closely related to the properties. Owing to their small size, colloidal particles exhibit unique properties distinct from bulk materials. For example, a high surface area to volume ratio increases surface energy of particles, resulting in outstanding catalytic activities [1–3]. The high surface area also enhances the solubility which is critical for pharmaceutical applications [4,5]. Moreover, the reduction in size significantly affects the electronic states of the particles [6,7]. In particular, the bandgap of semiconductor nanoparticles increases with a reduction in size, which is known as quantum confinement effect [8–10]. Colloidal particles also exhibit extraordinary properties including localized surface plasmon resonance [11,12], superparamagnetism [13,14], and photothermal effects [15,16], which can be engineered for specific applications. Dozens of metals [17,18], semiconductors [19–23], and polymers [24–26] have been used to synthesize colloidal particles, which are processed into various shapes such as spheres [27–30], cubes [31,32], rods [33,34], triangles [35,36], core-shells [37–39], and vesicles [40,41].

Superstructures of colloidal particles

By carefully adjusting the attractive and repulsive forces between the particles, colloidal particles spontaneously assemble into well-ordered superstructures including crystals, chains, and clusters [42,43]. Superstructures of colloidal particles are promising candidates for new nanomaterials because of their complicated structure and collective properties, which are not observed in individual particles. Colloidal crystals are ordered three-dimensional assemblies that resemble the crystalline structures of atomic crystals [44–46]. They are obtained by close-packing particles through evaporation of the solvent [47,48] or supramolecular interactions [49–51], and their crystalline structure is determined by the geometry of the constituent particles (Figure 1.1a) [47]. Owing to the crystallinity, they exhibit exceptional properties for functional materials, such as structural color arising from photonic crystals [52–54], high mobility carrier transport [55], and collective mechanical responses of coherent vibration [56,57]. In addition, colloidal particles can be close-packed at the interface of two phase, resulting in a two-dimensional superlattice [44,58]. Interestingly, non-close-packed two-dimensional superlattice of kagome structures have been also reported, obtained from the assembly of microspheres with two hydrophobic regions on the surface (Figure 1.1b) [59]. These planar colloidal superlattices are applicable for functional coatings such as surface enhanced Raman scattering

(SERS) [60,61]. In contrast to colloidal crystals and lattices, colloidal clusters, the aggregates of a few particles, independently disperse in the solvent [62]. The geometry of colloidal clusters can be delicately controlled from simple spheres to well-defined molecular mimetic structures by engineering the number of particles and clustering strategy (Figure 1.1c) [63–66]. The colloidal cluster can be further utilized as a building block for complex hierarchical materials, resulting from the step-wise assembly [67]. For example, the co-assembly of individual microsphere and tetrahedral clusters produces colloidal crystals of the $MgCu_2$ structure, which is extremely difficult to obtain [68]. In addition, colloidal clusters of particles with different functionalities can be utilized as multifunctional catalytic platforms [69,70].

1.1.2. Supracolloidal chains from linear assembly of colloidal particles

Supracolloidal chains are one-dimensional superstructures of colloidal particles. They span the gap between colloidal clusters and crystals, and show distinct behaviors from other superstructures owing to the linear structure. This chapter presents the assembly strategies of supracolloidal chains, the dipole-mediated and ligand-mediated assembly. Colloidal particles assemble into a linear supracolloidal chain through bidirectional attraction, while orthogonal repulsive forces prevent lateral aggregation.

Linear assembly from dipole-dipole interaction

The end-to-end attraction of magnetic and electrostatic dipoles can effectively induce the linear assembly of colloidal particles. In this strategy, undesirable aggregations from side-by-side attractions are suppressed by the van der Waals forces and steric repulsion of the surrounding ligands. Supracolloidal chains from dipolar interaction inherently respond to external fields, which affect their conformation, alignment, and movement.

Magnetic particles have been widely reported to form supracolloidal chains by using coupling interactions between magnetic dipoles [71,72]. For example, ferromagnetic nanoparticles of Co [73–75], Ni [76], Fe [77], and Fe_3O_4 [78] spontaneously assemble into chains, even in the absence of external magnetic fields (Figure 1.2a). These supracolloidal chains can be effectively stabilized by polymeric ligands, which prevent interchain aggregation through steric repulsion [79–81]. In addition, superparamagnetic particles can linearly assemble with the assistance of an external field, which enhances magnetic interaction to overcome the thermal fluctuation of dipoles [82–84]. The resulting chains are inevitably aligned parallel to the direction of field [72,85,86]. However, to obtain permanent chains, an additional crosslinking process is necessary because the field-induced dipoles immediately disappear without an external field [87,88].

Dipolar attraction between electrostatic dipoles also leads to linear assembly of particles. Since colloidal particles possessing inherent electrostatic dipoles are rarely reported [89,90], electrostatic dipoles should be induced on the building blocks before assembly. For example, oppositely charged particles first dimerize into dipolar monomers and then assemble in linear chains [91,92]. An external alternating current (AC) field can induce electrostatic dipole in colloidal particles, which can be utilized for their linear assembly (Figure 1.2b) [93,94]. Through the field-induced electrostatic dipoles, colloidal particles with various geometries such as spheres [95,96], ellipsoids [97], and Janus particles [98–100] have been reported to assemble into linear chains.

Linear assembly from attraction of surface patches

Introducing chemically and physically distinctive surface patches is a promising strategy for the assembly of supracolloidal chains. For bidirectional attraction, the number and geometry of patches are carefully engineered through phase separation of surface ligands or selective functionalization of anisotropic particles [101,102]. In general, each particle requires two patches for the bidirectional attraction, which provide attractive forces via a variety of chemistry such as hydrogen bonding, host-guest interaction, and solvophobic interactions [103–105].

Supramolecular interactions between molecular recognition pairs have been introduced to create attractive forces between patches [106,107]. Hydrogen bonding is a representative example of molecular recognition strategy utilized for assembly of patchy particles (Figure 1.2c) [108,109]. For example, hydrogen bonding between complementary single-stranded DNA strongly connects patchy particles with high specificity. DNA patches can be introduced on the surface of various particles, such as microbeads [110], metallic nanoparticles [65], and DNA origami [111]. Interestingly, chains of DNA-patchy particles show temperature-responsive behaviors because hydrogen bonding between DNA strands easily dissociates above a critical temperature [112]. Beyond hydrogen bonding, host-guest interactions [113,114], metal coordination [115,116], and zwitterionic interactions [117] have also been reported to induce attraction between patches for linear assembly.

Solvophobic interactions between patches can also mediate the linear assembly of supracolloidal chains. By making patches unfavorable to the solvent, particles assemble by combining the patches to reduce undesirable contact with solvent. For example, gold nanorods having hydrophobic patches at two ends were polymerized to a linear chain by merging the neighboring patches upon increasing the polarity of the solvent (Figure 1.2d) [118,119]. This solvophobic interaction is applicable to a variety of colloidal particles such as nanoplates [120], nanocubes [121], dimpled nanoparticles [122,123], and cylindrical micelles [124].

1.1.3. Property and application of supracolloidal chains

Owing to the synergetic interaction between particles and the highly anisotropic structure, supracolloidal chains show novel properties allowing various practical applications. This chapter first elucidates the plasmon and magnetic coupling of the chains, which originates from the synergetic interaction between particles, and then discusses the photonic crystals and mechanical behaviors from the perspective of structure related properties.

The supracolloidal chains of plasmonic nanoparticles show coupling behavior of surface plasmon resonance between the particles. Since the particles composing a chain are in proximity, plasmons are coupled with adjacent particles, resulting in a change in the transversal and longitudinal oscillation modes [125,126]. Specifically, the longitudinal plasmon resonance red-shifts as the chain length increases, which is further affected by the particle size and spatial gap between the particles (Figure 1.3a) [127,128]. This intimate relationship between the structure and plasmon coupling mode enables sensor application of the chains for detecting metal ions, organic molecules, and DNAs [116,129]. In addition, red-shifted extinction as the chain length can be utilized to quantitatively analyze the growth of the supracolloidal chain [130].

Through the coupling between magnetic dipoles, supracolloidal chains of magnetic particles show significantly enhanced magnetic properties, including large coercivity and anisotropic magnetization, which can be

utilized for high-density data storage, spintronics, and magnetic resonance imaging [71,131]. Furthermore, coupled dipoles lying in supracolloidal chains can control their arrays by aligning them parallel to an external field (Figure 1.3b) [80,132,133]. Moreover, when the chains are sufficiently flexible, they undergo a complex structural transformation under in the presence of an external field, which can induce field-adaptive motion [83,134]. The detailed applications of field-adaptive motion are discussed in the following paragraph on mechanical behavior. Interestingly, magnetotactic bacteria such as *magnetospirillum gryphiswaldense* uses supracolloidal chain of iron oxide nanoparticles to find low oxygen conditions from their responses to the magnetic field of the Earth [135].

Periodic arrays of dielectric colloidal particles, whose refractive indices differ from the environment, have photonic bandgaps, where the propagation of electromagnetic wave is only allowed for certain wavelengths [136,137]. Thus, the arrays emit structural color without the support of other emissive materials, whose wavelength is determined by the size and spatial period of the particles [138–140]. Because the particles are arranged in a linear fashion, supracolloidal chains exhibit structural color, which strongly depends on the angle between the direction of chains and the incident light (Figure 1.3c) [141,142]. Therefore, their structural color can be changed by adjusting the direction of aligned chains, implying their applications in

stimuli-responsive photonic crystals [143,144].

By affecting the velocity field of a fluid, one-dimensional nanostructures can cause significant changes in the rheological properties of the solution [145,146]. In a concentrated solution of magnetic particles, the viscosity dramatically increases when supracolloidal chains are formed by applying an external magnetic field, which is known as a magnetorheological fluid [147,148]. This phenomenon is also observed for the solution of supracolloidal chains fabricated by dipolar assembly of electric field-induced dipoles, called electrorheological fluid [149]. Magnetorheological and electrorheological fluids can be used in various mechanical engineering applications [150,151].

By engineering the motion, supracolloidal chains can be utilized as colloidal swimmers for microfluidics and nanorobotics. In particular, supracolloidal chains of magnetic particles undergo directional alignment or morphological transformation by responding to an external field, which can generate translational and rotational motions in solution [105]. For example, under a rotating magnetic field, chains of magnetic particles rotate and create a whirlpool, leading to the agitation of the solution. Thus, they can be utilized as nanoscale stirring bars for microscopic catalytic system and lab-on-a-chip system [152,153]. In addition, relatively flexible supracolloidal chains show structural transformation, such as stretched, folded and helical structures, as a response to the external field. By periodically transforming morphology

using a time-varying magnetic field, the chains can be propelled and behave as a micromotor through flagella-like motion (Figure 1.3d) [132,134,154].

1.1.4. Supracolloidal chains of block copolymer micelles

Block copolymer micelles

Block copolymers, in which chemically distinctive homopolymers are covalently linked, spontaneously assemble into ordered nanostructures through the segregation of dissimilar blocks. Block copolymers are classified by the number of component blocks, represented by diblock and triblock copolymers, and architectures of linear, star-like, and dendritic structures.

Block copolymers segregate into an ordered structure at the nanoscale, known as microphase separation [24,155]. This process is determined by the contributions of enthalpy and entropy of mixing, which are expressed by the Flory-Huggins interaction parameters (χ) and total degree of polymerization (N), respectively [156–158]. In bulk, the order-to-disorder transition of block copolymers is predicted by the product of the Flory-Huggins parameter and degree of polymerization (χN), which indicates the balance between enthalpy and entropy [156–158]. In particular, the simplest block copolymer system of diblock copolymers undergo microphase separation when χN exceeds 10.5. The nanostructures resulting from the microphase separation are determined by the volume fraction of each block

(f). For a diblock copolymer, by increasing the volume fraction of one block from 0 to 0.5, at a fixed χN, the nanostructure of the diblock copolymers varies from spherical to cylindrical, and subsequently to lamellar (Figure 1.4a) [156–158]. Block copolymers consisting of more than two blocks exhibit highly complex phase behaviors because the number of parameters involved in phase separation increases. For instance, triblock copolymers exhibit a broader spectrum of morphologies such as sphere-in-cylinder, double helices in cylinder, and core-shell cylinders [158–160].

When dissolved in a selective solvent for a certain block, the block copolymers aggregate into nanoscale micelles above the critical micelle concentration [161]. Generally, micelles have spherical, cylindrical, and vesicular morphologies, consisting of a soluble corona and an insoluble core. In solution assembly, the morphology of micelles is mainly determined by the volume fraction between the core- and corona-forming blocks, which is expressed by the packing parameter $p=v/a_0l_c$, where v and l_c denote the volume and length of the core-forming block, respectively, with a_0 indicating the contact area of the corona-forming block. Spherical micelles are obtained at a relatively low packing parameter ($p < 1/3$), whereas a higher packing parameter is required for cylindrical micelles ($1/3 < p < 1/2$) and vesicles ($1/2 < p$) (Figure 1.4b) [162,163]. In line with the bulk assembly, introducing an additional block increases the level of complexity, resulting in non-

conventional micellar morphologies such as core-shell structure and multicompartment micelles [158].

Supracolloidal chains of block copolymer micelles

Block copolymer micelles have been widely utilized as nanoscale building blocks for supracolloidal chains. To induce bidirectional attraction of the linear assembly, they are first converted into anisotropic patchy micelles by compartmentalizing the corona. The patchy micelles then assemble into linear supracollodial chains through solvophobic interactions between the surface patches [101,105,164]. The linear assembly of patchy micelles of polyethylene oxide-*b*-polystyrene-*b*-poly(2-vinylpyridine) triblock copolymer (PEO-*b*-PS-*b*-P2VP) is a typical example. PEO-*b*-PS-*b*-P2VP copolymers first aggregated into spherical micelles of the PS core and PEO/P2VP mixed corona. Upon increasing the solvent polarity, P2VP in the corona selectively collapsed, resulting in hydrophobic P2VP patches on the core. By further increasing the polarity of the solvent, the patchy micelles finally assembled into a linear chain through solvophobic interactions between P2VP patches (Figure 1.5a) [165]. This patchy micelle strategy has been utilized for diverse systems of diblock [166–169] and triblock copolymers [170–172] (Figure 1.5b and c). With a wide range of polymers for block segments, supracolloidal chains of block copolymer micelles with diverse

functionalities have been reported. For example, a light-induced assembly-disassembly system of the supracolloidal chain is obtained by introducing photochromic azobenzene moieties in a patchy block, whose polarity changes upon photoisomerization [173]. In addition, patchy micelles whose patches consist of a thermoresponsive poly(N-isopropyl-acrylamide) were assembled by increasing the temperature [172]. Moreover, functional materials such as nanoparticles [170,174], quantum dots [175], and organic dyes [176] can be incorporated into the micellar cores composing a chain.

1.1.5. Supracolloidal chains as nanoscale analogues of conventional polymers

Linear assembly of colloidal particles can be compared to polymerization of molecular monomers. In this regard, supracolloidal chains can be considered as colloidal analogues of conventional polymers. From this perspective, supracolloidal chains has been explained with the assistance of traditional theories of polymers. The analogy of supracolloidal chains and polymers can not only help us to understand their behaviors, which are crucial to design and fabricate supracolloidal chains with desired properties, but also provide inspirations for applications of the chains. Moreover, as supracolloidal chains can be directly visualized by microscopes, they can be utilized as a model system for polymer research.

Assembling mechanism of supracolloidal chains can be described by theories of polymerization. Because most of supracolloidal chains are assembled through bidirectional attraction of particles, their assembly processes have been extensively explained with step-growth mechanism, where the growth of chains follows the Carothers equation, and polydispersity index (PDI) approaches two [35,177–180]. It is noted that supracolloidal chains can also polymerize through a diffusion-controlled mechanism because of slow diffusion of particles [122,123,181–183]. Intriguingly, the chain-growth mechanism can describe the growth of the supracolloidal chains. For instance, supracolloidal chains of gold nanoparticles, which is induced by the sphere-to-cylinder transformation of the polymeric shell, share the characteristics of chain-growth polymers, whose colloidal monomers are only added to the end of a growing chain [184]. These understandings of assembling mechanism allow precise control of polymerization kinetics and resulting structures. Co-assembling colloidal monomers with different reactivities yields block-type supracolloidal chains [86,185,186], and colloidal monomers with more than three reactive groups induce branched chains and gels [187].

Flexibility and conformation of supracolloidal chains have been explained by the theoretical models of polymers. For the evaluation, physical dimensions of supracolloidal chains are first measured by the size parameters of conventional polymers including the contour length, persistence length,

end-to-end distance, and radius of gyration. The flexibility of supracolloidal chain can be assessed by comparing the persistence length with the contour lengths [82,188]. In particular, chains are assessed as rigid when persistence length exceeds contour length, and vice versa, they are flexible [189]. The flexibility information of supracolloidal chains is necessary for studying bending dynamics [87,190] and mechanical responses [190,191], which allows various applications such as colloidal liquid crystals [183], microdevices [191], and microswimmers [134,154]. Furthermore, conformation of supracolloidal chains has been successfully described by single chain models of polymers, including freely jointed chain [192] and worm-like chain model [190], which are determined by the flexibility of the chain.

1.2. Purpose of Research

1.2.1. Motivation

Supracolloidal chains have attracted increasing attention as one-dimensional nanomaterials for various applications. To design and fabricate supracolloidal chains with desired properties, it is crucial to understand how the chains are formed and behave. Because supracolloidal chains can be considered as a nanoscale analogue of conventional polymer, the chains can be described by the theory of conventional polymers. Moreover, the analogy of polymers provides inspiration for applications of the chains, such as processing and functionalization strategies.

1.2.2. Aim and objectives

This dissertation describes supracolloidal chains of patchy micelles of PS-*b*-P4VP as nanoscale analogues of a conventional polymer. The main purpose of this research is to understand assembling mechanism and single chain conformation of the chains and demonstrate application strategies by processing and functionalizing the chains. Assembling process is first elucidated using the mechanism of step-growth polymerization. Flexibility and conformation of the chains are explained using theoretical models of polymers, which are processed into a film. Finally, the PS-*b*-P4VP micelles

incorporating cobalt nanoparticles are demonstrated as functional colloidal monomers for supracolloidal chains.

In Chapter 2, assembling mechanism of the supracolloidal chains is discussed. Patchy micelles assemble into supracolloidal chains following the mechanism of conventional step-growth polymerization, where the degree of polymerization linearly increases and the polydispersity index approaches to two. According to the step-growth equation, a high degree of polymerization is achieved after a certain polymerization time by increasing the initial concentration of patchy micelles. Furthermore, cyclic supracolloidal chains are produced in a very low concentration. The colloidal polymerization is accelerated by adding more water to the solution and employing patchy micelles having large patches.

In Chapter 3, flexibility and conformation of the supracolloidal chains are elucidated. The persistence and contour lengths of supracolloidal chains coated on a solid substrate are assessed to evaluate their flexibility. Based on this analysis, the chain is semi-flexible, and the conformation is suitably explained by the worm-like chain model. In addition, a self-supporting film of supracolloidal chains with nanoscale pores is obtained by utilizing a spin-coating technique with semi-flexible chains.

In Chapter 4, PS-*b*-P4VP micelles incorporating cobalt nanoparticles are demonstrated as colloidal monomers of supracolloidal chains. By encapsulating CoNPs with PS-*b*-P4VP, spherical micelles incorporating

CoNPs are first prepared and then transformed into patchy micelles. The patchy micelles incorporating CoNPs are polymerized into supracolloidal chains. In this process, undesirable aggregation is prevented by treating P4VP shells with CH_3I.

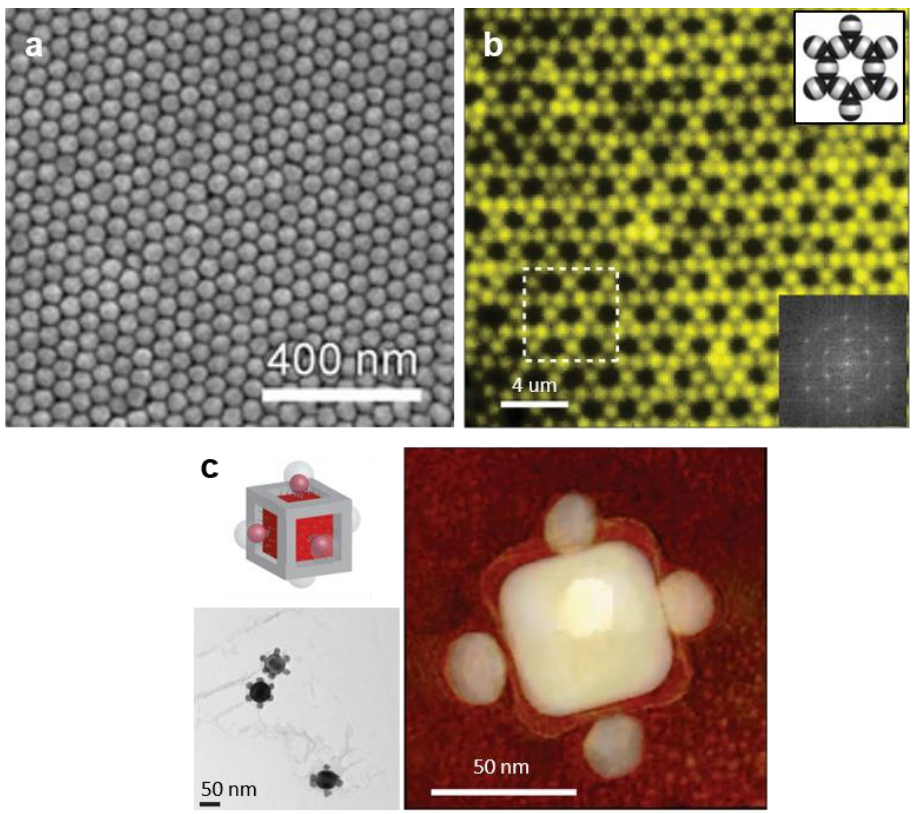

Figure 1.1 Superstructures of colloidal particles: (a) colloidal crystal [47]; (b) two-dimensional colloidal superlattice [59]; (c) colloidal cluster [65].

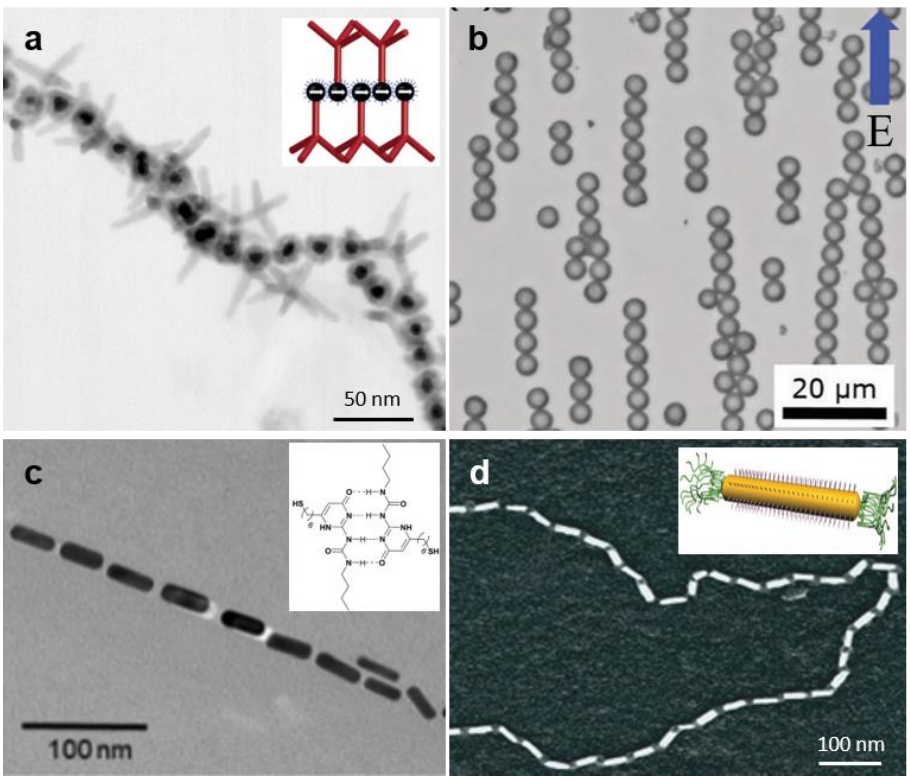

Figure 1.2 Supracolloidal chains from linear assembly of colloidal particles: (a) Magnetic dipolar interaction [75]; (b) Electrostatic dipolar assembly [95]; (c) Hydrogen bonding between patches [109]; (d) Solvophobic interaction between patches [118].

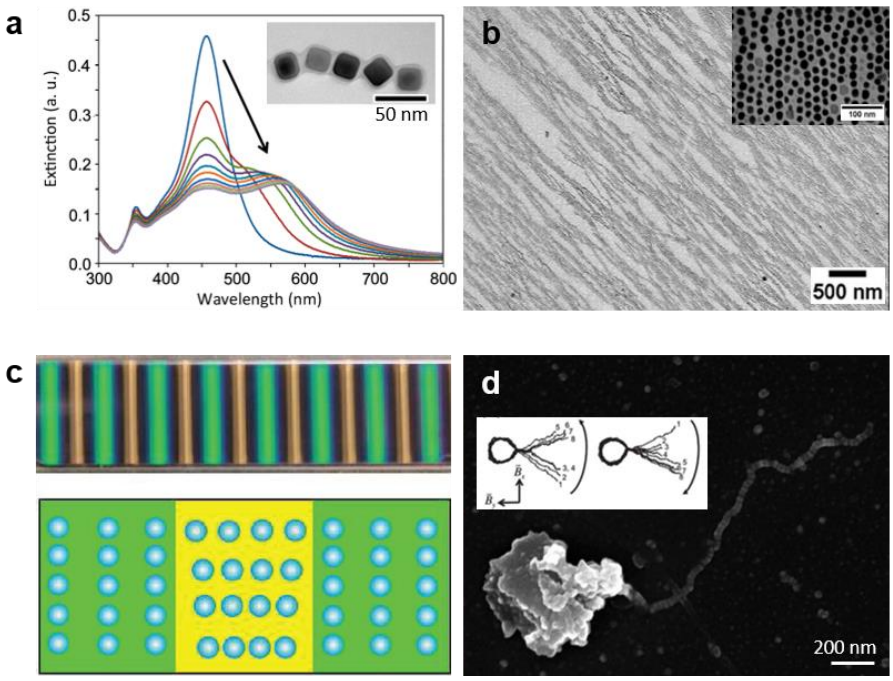

Figure 1.3 Properties of supracolloidal chains: (a) plasmonic coupling [128]; (b) magnetic coupling [80]; (c) one-dimensional photonic crystal [141]; (d) micromotor [132].

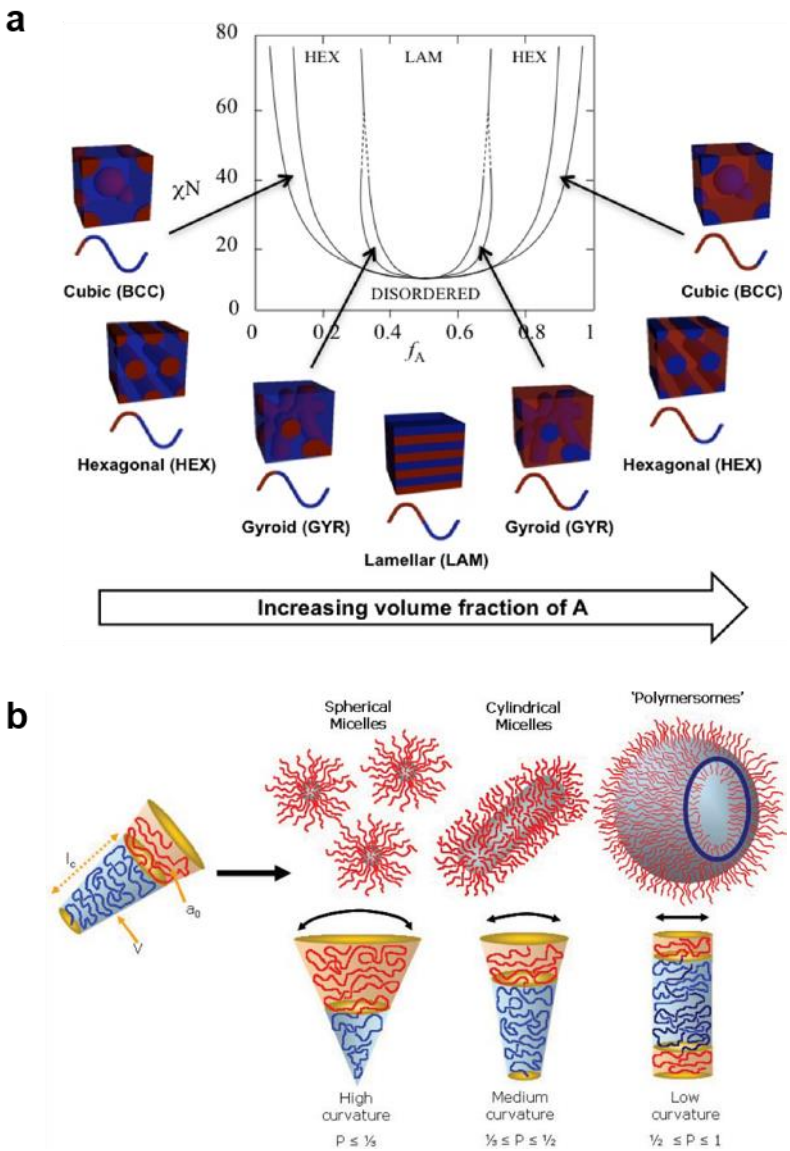

Figure 1.4 Self-assembled nanostructures of block copolymers: (a) bulk assembly [158]; (b) solution assembly [162].

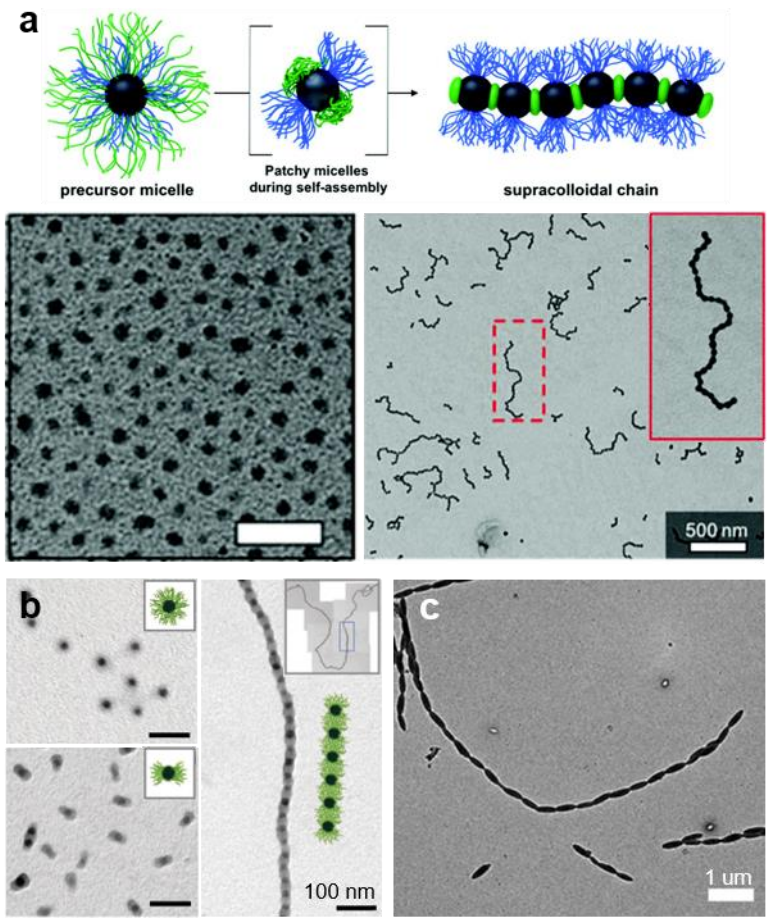

Figure 1.5 Supracolloidal chains of patchy micelles of block copolymers: (a) poly(ethyleneoxide)-*b*-polystyrene-*b*-poly(2-vinylpydine) [165]; (b) polystyrene-*b*-poly(4-vinylpyridine) [166]; (c) poly(γ-benzyl-L-glutamate)-*g*-poly(ethylene glycol) [169].

Chapter 2. Step−growth polymerization of patchy micelles of diblock copolymers

2.1. Introduction

Effective assembly of linear supracolloidal chains can be achieved by utilizing chemically or physically distinct patches on the surface of particles [65,104,193]. For example, gold nanorods having hydrophobic patches at two ends were polymerized to a linear chain by merging the neighboring patches upon increasing the polarity of the solvent [118]. In the same way, patchy micelles of triblock terpolymers, whose patches were originated from segregation in the corona, were assembled into a linear chain by combining the patches [165,170]. Moreover, patchy micelles were induced with diblock copolymers and assembled into linear supracolloidal chains [166,176,187], which can be further functionalized by incorporating nanoparticles and quantum dots in the cores of the micelles [174,175].

A supracolloidal chain consisting of colloidal monomers can be considered as a nanoscale analogue of a traditional polymer of molecular monomers [86,194]. In this perspective, the assembling mechanism of supracolloidal chains can be described by conventional theory of polymerization. For instance, the growth of supracolloidal chains from colloidal particles such as nanorods with patches [177] and patchy micelles of triblock terpolymers [181] was well explained by the mechanism of step-growth polymerization. In addition, chain-growth mechanism has explained the growth of supracolloidal chain assembled through morphological

transition of spherical micelles into cylindrical micelles [184]. The understandings of assembling mechanism allow engineering of the reaction kinetics and structures of supracolloidal chains. For example, co-assembling colloidal monomers with different reactivities yields block-type supracolloidal chains [86,185,186]. Furthermore, branched chains and networks have been demonstrated by introducing multifunctional colloidal monomers during the assembly, inspired by theory of gels [187].

In this study, assembling mechanism of supracolloidal chains of patchy micelles of PS-*b*-P4VP is demonstrated. Patchy micelles assembled into supracolloidal chains following the mechanism of conventional step-growth polymerization. By increasing the initial concentration, a high degree of polymerization was achieved after a certain time without changing the rate constants. In addition, cyclic supracolloidal chains were produced in an extremely diluted solution. Furthermore, the colloidal polymerization was accelerated by adding more water to the solution and employing patchy micelles having large patches.

2.2. Experimental Section

Materials: Polystyrene-*b*-poly(4-vinylpyridine) of PS(51)-*b*-P4VP(18) and PS(25)-*b*-P4VP(7) were purchased from Polymer Source, Inc. The numbers in the parenthesis are the number average molecular weights (M_n) in kg mol^{-}

[1]. The polydispersity indices (PDIs) are 1.15 and 1.10 for PS(51)-*b*-P4VP(18) and PS(25)-*b*-P4VP(7), respectively. Styrene (>99%), 4-vinylpyridine (95%), 2,2'-azobisisobutyronitrile (AIBN, 98%), 2-cyano-2-propy dodecyl trithiocarbonate (CPTTC, 97%), and 1,4-dibromobutane (99%) were purchased from Sigma-aldrich. CaH_2 (93%) was obtained from Acros Organics. Commercially available solvents and chemicals were used as received unless otherwise stated. The monomers were purified by the vacuum distillation from CaH_2 before polymerization. AIBN was recrystallized from diethylether.

Synthesis of PS-b-P4VP diblock copolymers: PS(145)-*b*-P4VP(40) was synthesized by reversible addition-fragmentation chain transfer (RAFT) polymerization as described in the literature [195]. The P4VP block was first synthesized and then utilized as a macro chain transfer agent (CTA) to synthesize the additional PS block. A mixture of 4VP (16.0 g), CPTTC (28 mg), AIBN (13 mg) was added into a 50 ml Schlenk tube and degassed by three freeze-pump-thaw cycles. The reaction mixture was then immersed in an oil bath at 80 ℃ for 1.5 h and subsequently cooled down in a water bath to stop the polymerization. The resulting mixture was diluted with dichloromethane (40 ml) and slowly poured into an excess of *n*-hexane (500 ml) to precipitate the polymer, which was collected by filtration and then

dried in a vacuum oven at room temperature for 1 day. The obtained P4VP (3.0 g) was used as a macro CTA for the synthesis of the second PS block. The above procedure of RAFT polymerization was repeated for PS(145)-*b*-P4VP(40). A mixture solution of styrene (3.0 g), macro CTA of P4VP (0.2 g), AIBN (0.08 mg), and DMF (3.2 g) were prepared and then the polymerization was proceeded at 110 ℃ for 24 h. The polymerized mixture was diluted with methylene chloride before precipitation in n-hexane. After precipitation, filtration, and drying, PS(145)-*b*-P4VP(40) (0.7 g) in pale yellow was obtained.

Formation of PS-b-P4VP micelles having the crosslinked cores: PS-*b*-P4VP (10 mg) was first dissolved in chloroform (3.0 g), a good solvent for both PS and P4VP blocks. Then, toluene (1.0 g), a selective solvent for the PS block, was slowly added to the solution. After mixing, chloroform was evaporated thoroughly at 50 ℃ and extra toluene was added to yield a 1.0 wt% toluene solution of PS-*b*-P4VP micelles. To crosslink the P4VP core, 1,4-dibromobutane (0.5 molar ratio to 4VP) was added to this solution, followed by stirring at 50 ℃ for 48h.

Preparation of patchy micelles as colloidal monomers: To produce patchy micelles, DMF (0.90 g) was added to a toluene solution (0.25 ~ 1.0 wt%, 0.10

g) of PS(51)-*b*-P4VP(18) micelles having the crosslinked cores. For PS(25)-*b*-P4VP(7) and PS(145)-*b*-P4VP(40), DMF was added to a 1.0 wt% toluene solution of core-crosslinked micelles, yielding a 0.01 wt% solution of patchy micelles.

Polymerization of patchy micelles: To polymerize patchy micelles into supracolloidal chains, we further increased the polarity of the solvent by adding a mixture of deionized water and DMF (2.5:7.5 w/w) to yield 12.5 (or 25.0) wt% water in the final solution. The solution was kept without stirring at 30 ℃ up to 48h.

Characterizations: NMR spectra were obtained on a Varian NMR System (500 MHz). Gel permeation chromatography (GPC) was carried out on an Agilent 1260 Infinity GPC system equipped with a PL gel 5-μm Mixed-D column (Agilent Technologies) and a differential refractive index detector. DMF with LiBr (0.01 M) was used as the eluent at a flow rate of 1.0 ml/min. A PS standard kit (Agilent Technologies) was used for the calibration. Scanning electron microscopy (SEM) was performed on a Carl Zeiss SUPRA 55VP at 2 kV and on a Hitachi S-4300 at 15 kV. SEM samples of supracolloidal chains were prepared by spin-coating (3000 rpm, 60 s) onto a Si wafer, followed by Pt coating. A Si wafer was cleaned using a piranha

solution (70:30 v/v of concentrated H_2SO_4 and 30% H_2O_2), and thoroughly rinsed with deionized water several times and then blow dried with nitrogen. Transmission electron microscopy (TEM) was performed on a Hitachi H-7600 at 100 kV. A TEM sample was prepared by dropping a solution of micelles or chains on a TEM grid with removal of excess solvent by a filter paper and drying in air. TEM samples were exposed to I_2 or RuO_4 vapor to stain P4VP or PS, respectively.

Evaluation of the degree of polymerization of supracolloidal chains: SEM images of supracolloidal chains were digitally processed by ImageJ software (NIH, USA) and then analyzed with Persistence software, a freely available Matlab script [196] to measure contour lengths. The number of micelles consisting a chain, *i.e.*, the degree of polymerization (x), was calculated by dividing contour length of a chain by a segment length of the patchy micelle, which are ~24 nm, ~32 nm, and ~43 nm for PS(25)-*b*-P4VP(7), PS(51)-*b*-P4VP(18), and PS(145)-*b*-P4VP(40), respectively. The number-average degree of polymerization ($\bar{x}_n$) was obtained from > 500 chains.

2.3. Results and Discussion

Supracolloidal chains were obtained by assembling patchy micelles of PS-*b*-P4VP diblock copolymers (Figure 2.1). PS(51)-*b*-P4VP(18) was first assembled into spherical micelles consisting of a PS corona and a P4VP core in toluene, a selective solvent for PS [166,174–176,187]. The P4VP cores of the micelles were then crosslinked with 1,4-dibromobutane [166,174–176,187]. The spherical shape of the micelles was recognized in the TEM images, in which the cores and coronas appeared dark after stained with I_2 and RuO_4, respectively (Figure 2.2). Upon the addition of DMF to a toluene solution of PS-*b*-P4VP micelles, two patches were induced on a spherical micelle by segregating the corona. The cross-linked P4VP core cannot be dissolved by a favorable solvent of DMF. However, the P4VP core can be exposed to DMF by rearranging the PS corona into two separate patches, resulting in a dumbbell-shaped structure of two divided PS patches connected with the exposed P4VP core [166,174–176,187]. Patchy micelles in a dumbbell shape are clearly visible in the TEM and SEM images (Figure 2.3, top row). By taking a close look at the micelles in Figure 2.3a, the core, which remain spherical after patch formation, is observed between two patches. The patches look plump in the TEM image of Figure 2.3b after RuO_4 staining, similar to the SEM image of Figure 2.3c. It is noted that the line in the center correspond to the exposed core.

By adding water to a solution of the patchy micelles which can be considered as colloidal monomers, patchy micelles polymerized into supracolloidal chains. The addition of a polar solvent reduces the solubility of the hydrophobic patches so that attraction between the patches of neighboring micelles occurs, leading to polymerization of patchy micelles into a chain [166,174–176,187]. Lateral aggregation of the colloidal monomers can be effectively prevented by the P4VP core exposed to the solvent because the exposed P4VP core becomes more favorable to contact with the solvent containing water. In addition, bonding between the micelles is created by fusing two patches of neighboring micelles so that the patch works as a reactive functional group. Thus, with the micelle having two patches, a colloidal analogue of a bifunctional monomer, a linear supracolloidal chain can be dominantly produced. A supracolloidal chain is shown in the TEM image of Figure 2.3d, where the spherical cores located along the chains are observable after I_2 staining. The TEM image obtained after RuO_4 staining (Figure 2.3e) and the SEM image (Figure 2.3f) also shows a supracolloidal chain, which looks like a string of beads and resembles a rosary. Along the chain, lines, corresponding to the cores, are clearly discerned between the beads that are the fused patches after merging two patches of neighboring micelles, which appear dark in the TEM image due to RuO_4 staining. In addition, two chain ends, which are uncombined patches so that they are

smaller than fused patches, can be found in both images of Figure 2.3e and 2.3f. It is worthwhile to note that the degree of polymerization (x) can be directly obtained by counting the number of cores in the chain. However, an approximate x was employed by dividing the contour length by the segment length (~32 nm) in the following discussion.

The assembling mechanism of the patchy micelles can be explained by the step-growth polymerization. Thus, it is first investigated that whether the distribution of x follows the most-probable distribution, which is a characteristic of the step-growth mechanism [197]. By spin-coating supracolloidal chains from a dilute solution (2.50 x 10^{-2} wt%), well-separated chains with sufficient numbers (> 1200) are found for the analysis of size distributions in large-area SEM images, parts of which are shown in Figure 2.4. As the polymerization proceeded (0.5 h to 6 h), chains apparently became longer in the SEM images of Figure 2.4, which can be verified by the increase of the number of longer chains in the size distributions. Each distribution follows the most-probable distribution of $N_x=p^{x-1}(1-p)$, where N_x is the number fraction of chains having x and p is the extent of reaction, marked as the green lines, confirming a feature of the step-growth polymerization [197].

From each distribution in Figure 2.4, the number-average degree of polymerization ($\bar{x}_n$) and polydispersity index (PDI) were calculated, which were plotted with respect to the polymerization time (Figure 2.5). As the polymerization proceeded, $\bar{x}_n$ linearly increased and PDI gradually

approached to two, which are well fitted with the conventional step-growth equations of $\bar{x}_n$=1+$2k$[A]$_0t$ and PDI=2–1/$\bar{x}_n$, respectively [197]. It is noted that [A]$_0$ is the initial molar concentration of colloidal monomers, which was evaluated as 1.77×10^{-8} mol L^{-1} by dividing the total weight of polymers in a solution by the weight of one micelle estimated from the micelle size. From the slope in Figure 2.5a, the rate constant (k) were calculated as 1.67×10^4 M^{-1} s^{-1}, which is much greater than the typical values (10^{-5}~10^{-3} M^{-1} s^{-1}) for small molecules [197] but shows a similar order of magnitude to those (10^4~10^5 M^{-1} s^{-1}) found in the polymerization of nanoscale particles [122,177].

To achieve a high $\bar{x}_n$ after a certain polymerization time, the initial concentration [A]$_0$ can be simply increased according to the conventional step-growth equation of $\bar{x}_n$=1+$2k$[A]$_0t$. Figure 2.6 shows the distributions of x of supracolloidal chains after 6 h by varying the initial concentration. The chains in a higher concentration appear longer in the SEM images of Figure 2.6, which can be identified in the size distributions. It is noted that all distributions follow the most-probable distribution of the step-growth polymerization regardless of the initial concentration. Figure 2.7a also shows the linear increase of $\bar{x}_n$ as the polymerization proceeded with a larger slope for a higher initial concentration. From these slopes, the rate constant k was obtained by plotting d$\bar{x}_n$/dt vs. [A]$_0$ (Figure 2.7b), which is 1.68×10^4 M^{-1} s^{-1}, not changed with the variation of the initial concentration. It is noteworthy

that the linear dependence of $\bar{x}_n$ on the polymerization time and the concentration-independent rate constant k imply the insignificant effect of diffusion on the polymerization [122,197].

In conventional step-growth polymerization, a high concentration of monomers is desirable in order to minimize the cyclization by intramolecular reaction [197]. In contrast, a very low concentration (2.50×10^{-4} wt%) of patchy micelles was intentionally employed for the formation of a cyclic chain, which cannot be easily detected in polymerization of small molecules. As the result, several neckless structures with various sizes were observed in the TEM image of Figure 2.8. The enlarged image in the inset clearly shows a closed-loop of beads on a string, indicating a cyclic supracolloidal chain originated from merging of the two end patches in the same chain due to a low concentration of colloidal monomers [197].

Colloidal polymerization of patchy micelles is mainly progressed by merging the non-polar PS patches on the neighboring micelles to reduce the unfavorable contact with the polar environments after addition of water, implying that more water can accelerate the polymerization. Twice amount of water was added to a solution of the patchy micelles having the same initial concentration. After 3h polymerization (Figure 2.9a), the chains polymerized with more water apparently appear longer. $\bar{x}_n$ were again plotted with respect to the polymerization time for two different water contents. Figure 2.9b shows a larger slope for a high content of water. The rate constant is also

evaluated as 2.84×10^4 M^{-1} s^{-1}, indicating 1.6 times faster polymerization by adding twice amount of water.

The fast polymerization of the patchy micelles in an environment with a high content of water implies that the polymerization can be accelerated if we employ a micelle with a large patch because the solubility of a polymer decreases with the increase of its molecular weight [198]. Thus, two independent patchy micelles having the dissimilar patch sizes were prepared by utilizing PS(25)-*b*-P4VP(7) and PS(145)-*b*-P4VP(40) (Figure 2.10). Both PS-*b*-P4VP block copolymers assembled into spherical micelles in toluene (Figure 2.11), from which the patchy micelles were induced as shown in the TEM images of Figure 2.12. As before, the patchy micelles of both PS(25)-*b*-P4VP(7) and PS(145)-*b*-P4VP(40) have a dumbbell-like shape. However, the patchy diameter (~42 nm) of PS(145)-*b*-P4VP(40) is twice larger than that (~23 nm) of PS(25)-*b*-P4VP(7), indicating the quadruple difference in the surface areas. Both patchy micelles were polymerized into supracolloidal chains, which appear as beads on a string in the SEM images of Figure 2.12. The chain of PS(145)-*b*-P4VP(40) is much thicker than that of PS(25)-*b*-P4VP(7). Again, $\bar{x}_n$ was investigated with respect to the polymerization time (Figure 2.13). The initial molar concentration of the patchy micelles is 7.72×10^{-9} M for PS(25)-*b*-P4VP(7) and 1.59×10^{-9} M for PS(145)-*b*-P4VP(40). The polymerization of both patchy micelles follows the linear

relation of $\bar{x}_n$=1+$2k$[A]$_0t$. The rate constant (1.76 × 10^4 M^{-1} s^{-1}) of the large patchy micelles is approximately twice higher than that (0.92 × 10^4 M^{-1} s^{-1}) of the small ones, confirming the fast polymerization with the micelles having the large patches.

2.4. Conclusion

Patchy micelles of PS-*b*-P4VP, which can be considered as bifunctional colloidal monomers, polymerized into supracolloidal chains following the mechanism of step-growth polymerization, where $\bar{x}_n$ linearly increases and PDI approaches to two. According to the conventional step-growth equation, a high $\bar{x}_n$ was achieved after a certain polymerization time by increasing the initial concentration of patchy micelles. In this process, the rate constant k remains unchanged, implying negligible effect of diffusion on the polymerization. Furthermore, cyclic supracolloidal chains were produced in a very low concentration, which are hardly detected in conventional polymers. The colloidal polymerization was accelerated by simply adding more water to the solution since the chain formation is induced by the unfavorable contact of patches with water. The fast polymerization was also accomplished by employing patchy micelles having large patches. Thus, the reactivity of colloidal monomers was effectively engineered by modifying chemical environment and patch size, which can be extended to colloidal reaction of

patchy particles for colloidal molecules. The colloidal polymerization approach demonstrated here provides not only the theoretical explanation for the assembling process but also synthetic strategy for supracolloidal chains with controlled kinetics and structures.

Figure 2.1 Schematic illustration of linear assembly of supracolloidal chains of PS-*b*-P4VP micelles

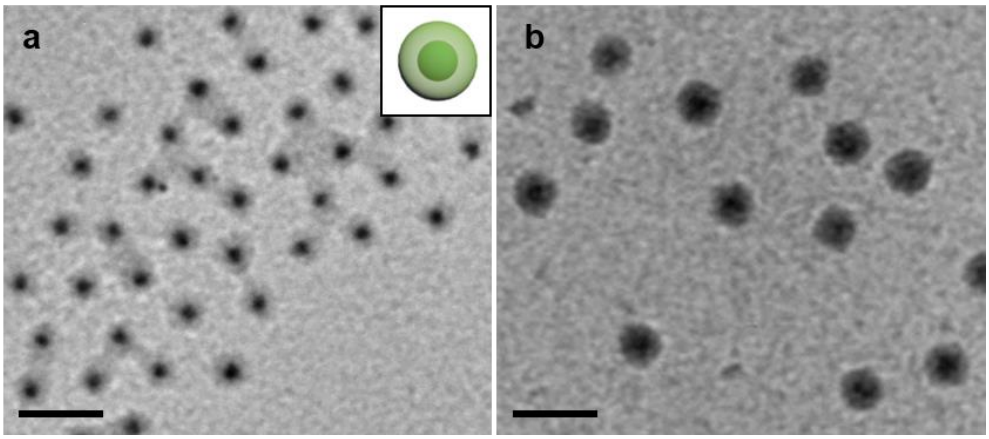

Figure 2.2 TEM images of spherical micelles of PS(51)-*b*-P4VP(18): (a) after staining P4VP with I_2; (b) after staining PS with RuO_4. The scale bars are 100 nm. Schematic illustration of a spherical micelle is depicted in the inset of (a).

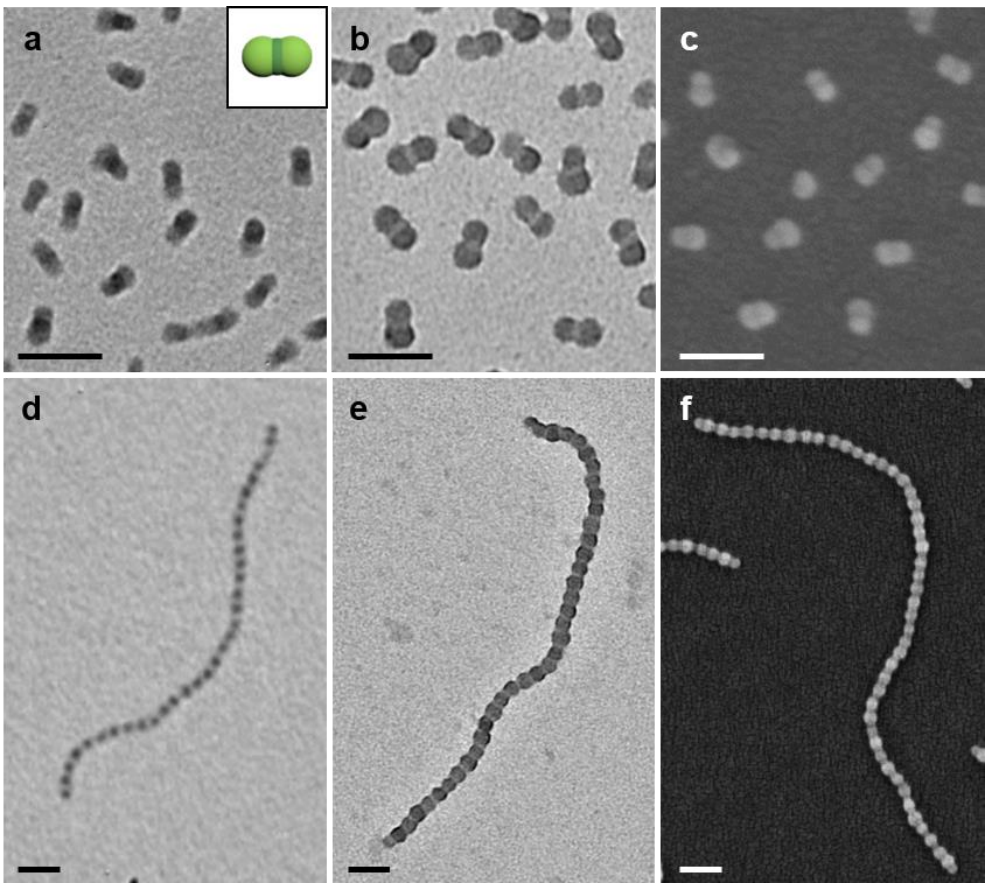

Figure 2.3 Patchy micelles (top row) and supracolloidal chains (bottom row) of PS(51)-*b*-P4VP(18): (a) and (d) TEM image after staining P4VP with I_2; (b) and (e) TEM image after staining PS with RuO_4; (c) and (f) SEM image. The scale bars are 100 nm. Schematic illustration of a patchy micelle is depicted in the inset of (a).

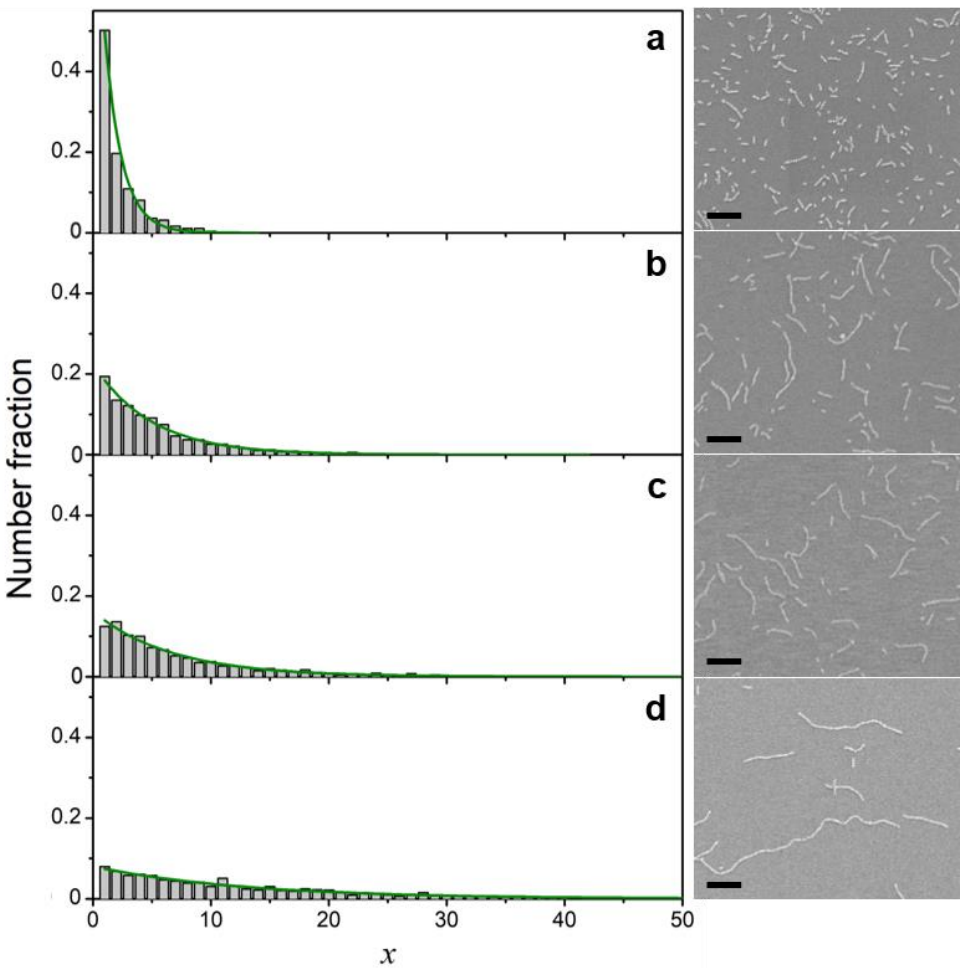

Figure 2.4 Distributions of degree of polymerization *x* of supracolloidal chains after polymerization: (a) 0.5 h; (b) 2 h; (c) 3 h; (d) 6 h. The corresponding SEM images are placed on the right with the scale bar of 500 nm. The green lines are the most-probable distributions, from which the extent-of-reaction values for 0.5 h, 2 h, 3 h, and 6 h are extracted as 0.50, 0.82, 0.86, and 0.93, respectively.

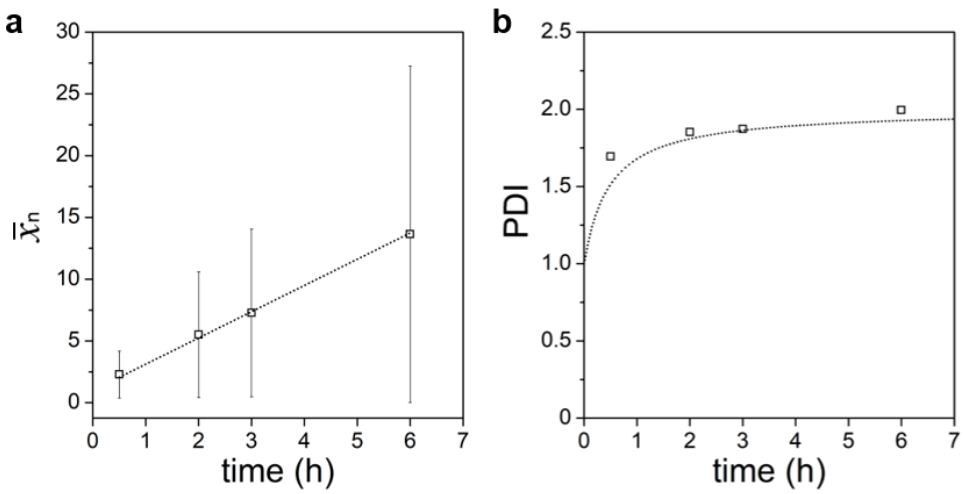

Figure 2.5 Evolution of $\bar{x}_n$ and PDI during polymerization: (a) $\bar{x}_n$; (b) PDI. The dotted lines in (a) and (b) are calculated by the conventional step-growth equations of $\bar{x}_n$=1+$2k$[A]$_0t$ and PDI=2−1/$\bar{x}_n$, respectively. The error bars indicate the standard deviations of counting.

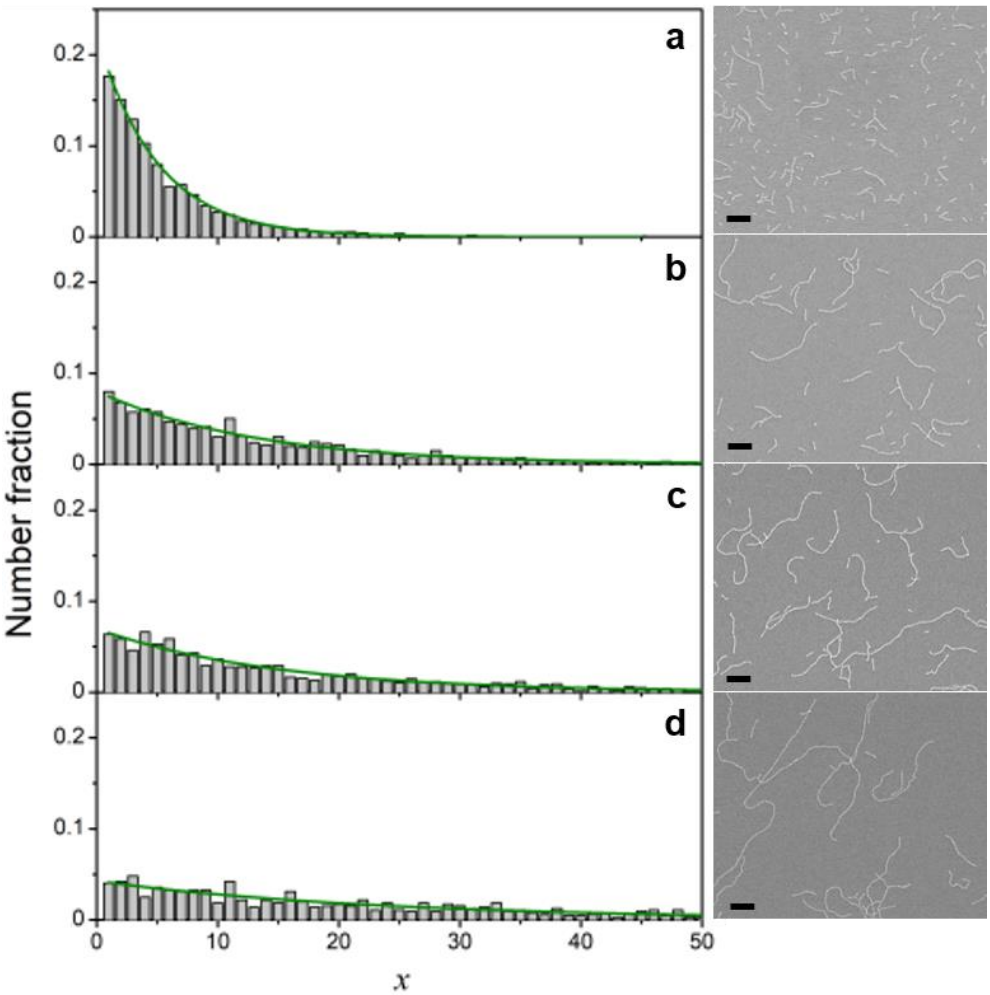

Figure 2.6 Distributions of degree of polymerization *x* of supracolloidal chains after 6 h by varying the initial concentration: (a) 1.25×10^{-2} wt%; (b) 2.50×10^{-2} wt%; (c) 3.75×10^{-2} wt%; (d) 5.00×10^{-2} wt%. The corresponding SEM images are placed on the right with the scale bar of 500 nm. The green lines are the most-probable distributions.

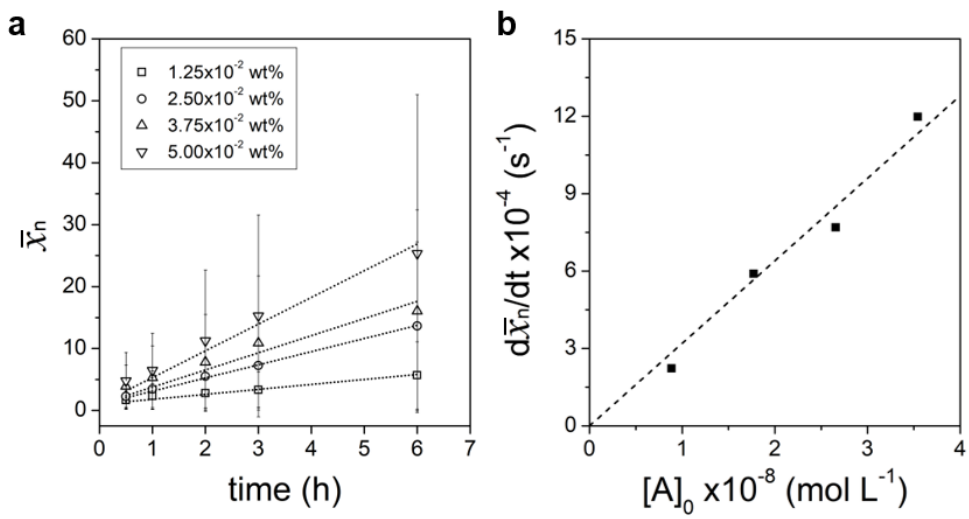

Figure 2.7 Polymerization of supracolloidal chains by varying the initial concentration: (a) $\bar{x}_n$ vs. time; (b) $d\bar{x}_n/dt$ vs. $[A]_0$. The dotted lines in (a) are calculated by $\bar{x}_n = 1 + 2k[A]_0 t$. The error bars in (a) indicate the standard deviations of counting.

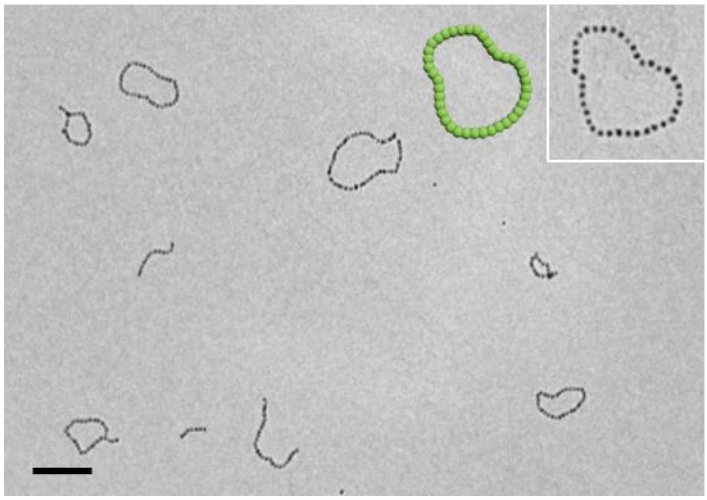

Figure 2.8 TEM image of cyclic supracolloidal chains after staining with I_2. The scale bar is 500 nm. The inset is an enlarged image of a representative cyclic chain in 600 nm × 600 nm. Schematic illustration of the cyclic chain is given at the left of the inset.

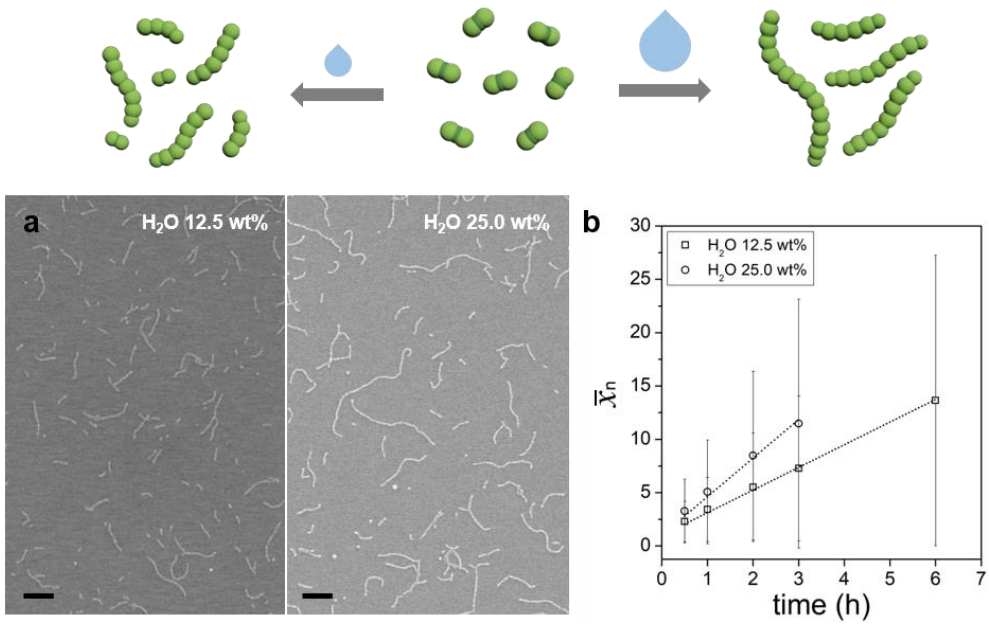

Figure 2.9 Effect of the content of water on polymerization of patchy micelles: (a) SEM images after 3h polymerization with the scale bar of 500 nm; (b) $\bar{x}_n$vs. time. The dotted lines in (c) are calculated by $\bar{x}_n$=1+$2k$[A]$_0t$. The error bars in (c) indicate the standard deviations of counting. Schematic illustration is given above the images.

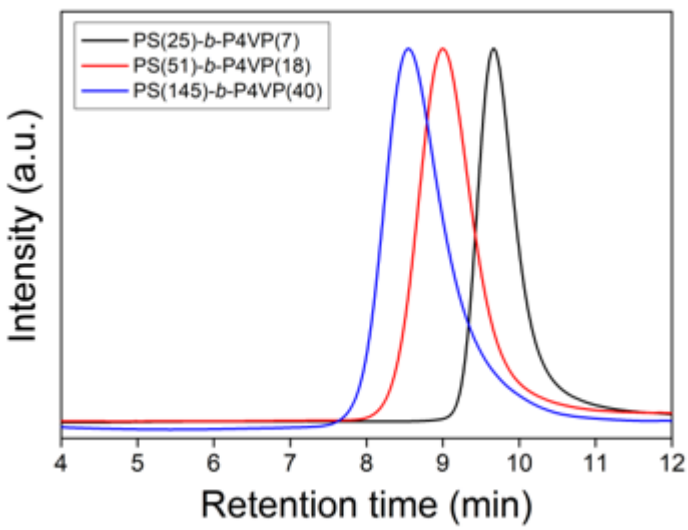

Figure 2.10 GPC results of PS-*b*-P4VP used for assembly of supracolloidal chains.

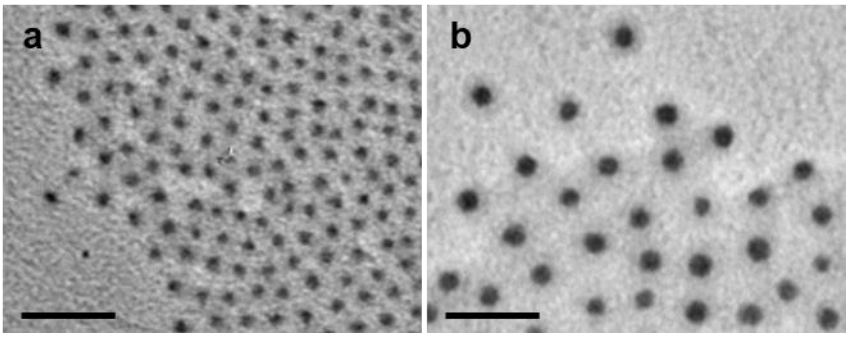

Figure 2.11 TEM images of spherical micelles: (a) PS(25)-*b*-P4VP(7); (b) PS(145)-*b*-P4VP(40). TEM images were obtained after stained with I_2. The scale bars are 100 nm.

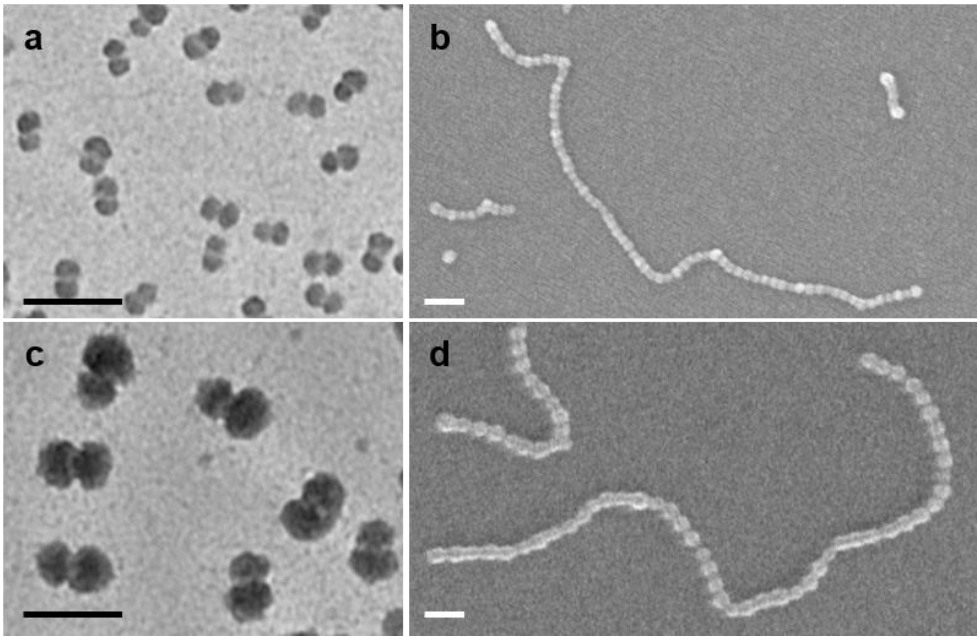

Figure 2.12 Colloidal polymerization of PS(25)-*b*-P4VP(7) (top row) and PS(145)-*b*-P4VP(40) (bottom row): (a) and (c) TEM images of patchy micelles after staining with RuO_4; (b) and (d) SEM images of supracolloidal chains. The scale bars are 100 nm.

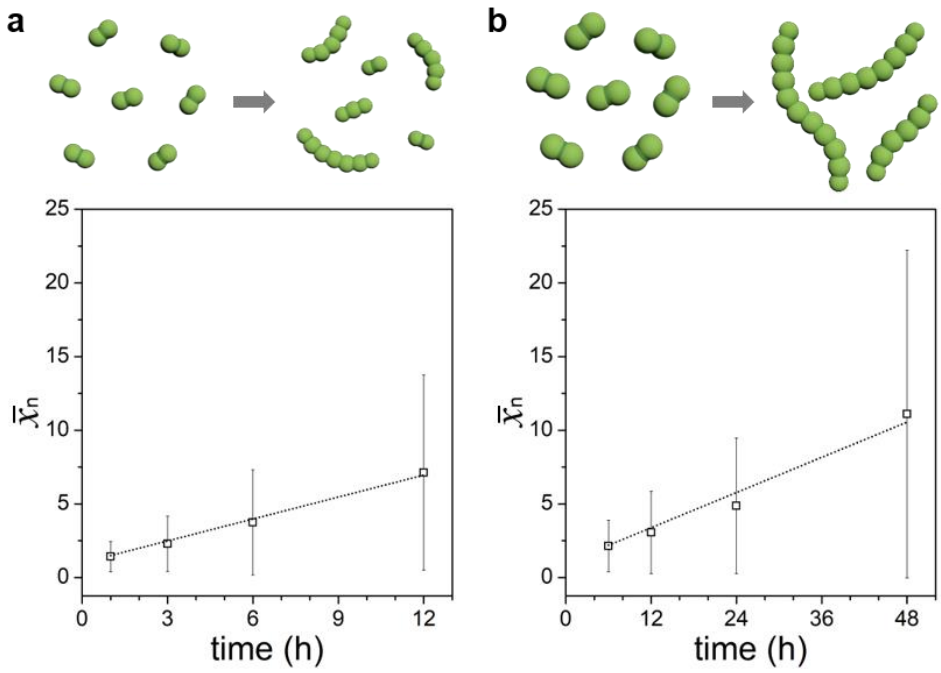

Figure 2.13 Evolution of $\bar{x}_n$ for patchy micelles with different size of patches: (a) PS(25)-*b*-P4VP(7); (b) PS(145)-*b*-P4VP(40). The dotted lines are calculated by $\bar{x}_n = 1 + 2k[\mathrm{A}]_0 t$. Error bars indicate standard deviations of counting. Schematic illustrations are given above the corresponding graphs of $\bar{x}_n$ vs. time.

Chapter 3. Porous self−supporting film of semi−flexible supracolloidal chains of diblock copolymer micelles

3.1. Introduction

To understand physical and mechanical behaviors of supracolloidal chains, it is crucial to understand their flexibility [154,189]. For a conventional polymer, flexibility determines not only conformations of single chain but also mechanical properties of bulk materials such as elastic modulus and crystallinity [198]. Based on the analogy of polymers, flexibility of supracolloidal chains can be also determined by using theoretical tools of polymers [190,199]. The physical dimensions of chains are first measured in the traditional parameters of polymers such as radius of gyration and end-to-end distance [80,192]. Then, flexibility and bending rigidity of supracolloidal chains can be evaluated by comparing their persistence length and contour length [154,188,189]. Flexibility of supracolloidal chains allows to investigate their physical behaviors such as conformation, alignments, and mechanical responses [134, 183, 192, 199].

Owing to high aspect ratio, one-dimensional nanomaterials including nanowires and supracolloidal chains have been processed into macroscopic films with microscopic percolation networks similar to conventional polymers [200–202]. These films have been developed for various applications such as flexible and stretchable devices, which show unique mechanical behaviors with novel properties [203,204]. However, there are few example of film formation from supracolloidal chains [205].

In this study, flexibility, conformation, and processing of the supracolloidal chains are elucidated. The flexibility of supracolloidal chains was first assessed by evaluating their persistence lengths and contour lengths. Based on the analysis, the chains were semi-flexible, and their conformation was suitably explained by the worm-like chain model. Then, by utilizing spin-coating process with the semi-flexible nature of chains, a self-supporting film of supracolloidal chains having microscopic pores was obtained, which would not be easily achievable with colloidal particles due to their tendency toward dense packing.

3.2. Experimental Section

Materials: Polystyrene-*b*-poly(4-vinylpyridine), PS-*b*-P4VP, with a number average molecular weight (M_n) of 51,000 g mol^{-1} for PS and 18,000 g mol^{-1} for P4VP and polydispersity index (PDI) of 1.15, was purchased from Polymer Source. Commercially available solvents and chemicals were used as received. 1,4-dibromobutane was purchased from Sigma-Aldrich.

Formation of PS-b-P4VP micelles and crosslinking of P4VP cores: PS-*b*-P4VP (10 mg) was first dissolved into chloroform (3.0 g), a good solvent for both PS and P4VP blocks. Then, toluene (1.0 g), a selective solvent for the PS block, was slowly added to the solution. After mixing, chloroform was

evaporated thoroughly at 50 ℃ and extra toluene was added to yield a 1.0 wt% toluene solution of PS-*b*-P4VP micelles. To crosslink the P4VP core, 1,4-dibromobutane (2.7 mg, 0.5 molar ratio to 4VP) was added to this solution, followed by stirring at 50 ℃ for 48h.

Preparation of patchy micelles and supracolloidal chains: To produce colloidal monomers of patchy micelles, DMF (0.99 g) was added to a 1.0 wt% toluene solution of core-crosslinked micelles (0.01 g), resulting in a 0.01 wt% solution of patchy micelles. To polymerize the patchy micelles into supracolloidal chains, a mixture of deionized water and DMF (2.5:7.5 w/w) was added to the solution of patchy micelles to yield 12.5 wt% water in the final solution. The solution was kept without stirring at 30 ℃ for 24 h.

Spin-coating and transferring of supracolloidal chains: A silicon wafer with a thermally grown oxide layer with a thickness of 300 nm (Si/SiO_2) was cleaned using a piranha solution (70:30 v/v of concentrated H_2SO_4 and 30% H_2O_2), and thoroughly rinsed with deionized water several times and then blow dried with nitrogen. The solution of supracolloidal chains was spin-coated onto a cleaned substrate at 3000 rpm for up to 200 repeats. The supracolloidal chains prepared after 200 cycles of spin-coating were floated

on water by dissolving the underlying SiO_2 layer with a 2.0 M aqueous solution of sodium hydroxide and transferred onto another Si/SiO_2 wafer.

Characterizations: Scanning electron microscopy (SEM) was performed on a Carl Zeiss SUPRA 55VP at 2 kV and on a Hitachi S-4300 at 15 kV. SEM samples of patchy micelles of PS-*b*-P4VP on a Si/SiO_2 substrate were prepared by spin-coating followed by Pt coating. Transmission electron microscopy (TEM) was performed on a Hitachi H-7600 at 100 kV. A TEM sample was prepared by dropping a solution of micelles or chains on a TEM grid with the removal of excess solvent by filter paper and drying in air. The TEM samples were exposed to I_2 or RuO_4 vapor to stain P4VP or PS, respectively.

Conformational analysis of supracolloidal chains: SEM images of supracolloidal chains were digitally processed using ImageJ software (NIH, USA) and then analyzed with Persistence software, a freely available Matlab script [196] to evaluate contour length (L), end-to-end distance (R_e), and persistence length (L_p). The radius of gyration (R_g) of each chain was also calculated by Equation 3.1 from its contour coordinates (x, y) consisting of N segments, depending on its length.

$$R_g = \sqrt{\frac{1}{N}\sum_i \left[(x_i - \frac{\sum_i x_i}{N})^2 + (y_i - \frac{\sum_i y_i}{N})^2\right]} \qquad (3.1)$$

3.3. Results and discussion

Supracolloidal chains were polymerized by assembling patchy micelles of PS-*b*-P4VP, which can be considered as colloidal monomers, by applying same protocol demonstrated in Chapter 2. Patchy micelles were first prepared by adding DMF to a toluene solution of core-crosslinked spherical micelles of PS-*b*-P4VP (Figure 3.1). The TEM image of Figure 3.1b shows patchy micelles of PS(51)-*b*-P4VP(18) in a dumbbell shape, where two hemispherical PS patches are connected by the P4VP core. The patch formation was explained as the result of segregation of the PS corona due to the preferential swelling of the cross-linked P4VP core by DMF [166]. These patchy micelles assembled into supracolloidal chains by addition of water to a solution of patchy micelles. As shown in the SEM in Figure 3.2, a long chain is observed as like beads on a string, which can be also identified in the TEM images (Figure 3.2b and c). The chain formation of colloidal polymerization can be described by merging the non-polar PS patches on the neighboring micelles in order to reduce the unfavorable contact with water [166]. Along the chain in Figure 3.2a, the beads correspond to the merged patches. The two chain ends, which are unreached patches without merging, appear smaller. It is worthwhile to note that dimers are also observed in Figure 3.2a, which consists of one bead and two ends. In this regard, the degree of polymerization x of a chain can be directly obtained by counting the number of beads, which

is 35 for the chain in Figure 3.2a. For evaluating *x* in the following analysis, however, the contour length of each chain in an SEM image was divided by the length of the repeating unit (~32 nm) as discussed in Chapter 2. In this chapter, supracolloidal chains were fabricated in a relatively low concentration (0.005 wt%), to clearly observe each chain without overlap in order to analyze their conformation.

As conventional polymers can be processed to form a film upon coating from their solutions, supracolloidal chains were spin-coated onto a substrate. After one-time spin-coating, scattered chains with negligible overlaps were found due to the low concentration (0.005 wt%) of the solution (Figure 3.3). The chains had various lengths and were randomly oriented in the image of Figure 3.3. The contour lengths of 1085 individual chains were measured from the SEM images. Figure 3.4a shows a histogram of the contour lengths of chains, in which the number of chains drastically decreases as the contour length increases. The number- and weight- averages of contour lengths are calculated by $L_n = \sum_i n_i l_i / \sum_i n_i$ and $L_w = \sum_i n_i {l_i}^2 / \sum_i n_i l_i$, respectively, giving L_n = 400 nm and L_w = 854 nm, where *l* is the length of a chain and *n* is the number of chains with length *l*. The polydispersity index (PDI) of L_w/L_n is 2.13, close to 2, implying that the chain formation can be explained by the step-growth mechanism in consistent with the Chapter 2. Since DPs in step-growth polymerization follow the most probable distribution, contour lengths and counting numbers are converted to DPs and

number fractions of the total, respectively, as shown in Figure 3.4b. The dotted line is a fitting curve of $p^{n-1}(1-p)$ with an extent of reaction p of 0.90 (R^2=0.943), where n is the DP of each chain, offering additional evidence of the step-growth mechanism for the chain formation [177]. It is noted that the most probable distribution of chain lengths deviates from the normal distribution of sizes observed in non-directional colloidal assemblies.

Since the chains shown in Figure 3.3 are somewhat extended, the persistence length (L_p) was evaluated from the correlation between the tangent angles along the chain to assess the flexibility of supracolloidal chains. As before, 1085 chains were used to calculate the average cosine correlation $\langle C(s)\rangle = \langle \cos[\theta(s) - \theta(0)]\rangle$, where s and $\theta(s)$ are the distance from the chain end to a point along the chain and the tangent angle at the point, respectively. Then, L_p of 546 nm was obtained by fitting the correlation with the two-dimensional case of $\langle C(s)\rangle = A\exp(-s/2L_p)$, where A is a scaling factor [83,196]. Since this persistence length is comparable to the average contour length (L_n = 400 nm, L_w = 854 nm), it can be stated that supracolloidal chains are semi-flexible [189]. It is noted that the value of L_p here is larger than that of double-strand DNA (~50 nm) [206] but smaller than that of an actin filament (> 9 um) [207]. The semi-flexibility of supracolloidal chains was further investigated with the worm-like chain model, in which the radius of

gyration (R_g) and the end-to-end distance (R_e) as a function of contour length (L) can be described by Equations 3.2 and 3.3, respectively [208].

$$R_g = \left[\frac{2}{3}L_pL - 4{L_p}^2 + \frac{32{l_p}^4}{L^2}\left(\exp\left[-\frac{L}{2L_p}\right] - 1\right) + \frac{16{L_p}^3}{L}\right]^{\frac{1}{2}} \quad (3.2)$$

$$R_e = 4L_pL - 8{L_p}^2\left(1 - \exp\left[-\frac{L}{2L_p}\right]\right) \quad (3.3)$$

It is noteworthy that Equations 3.2 and 3.3 are modified versions for a worm-like chain on a two-dimensional flat surface. Again, the values of R_g, R_e, and L for 1085 chains were extracted from the SEM images as explained in the experimental section. As shown in Figure 3.5, R_g and R_e against L are marked as open circles. Then, Equations 3.2 and 3.3 with L_p = 546 nm are plotted as the dotted lines in Figures 3.5a and 3.5b, respectively. The extracted values of both R_g and R_e from the images are well fitted with the equations, implying that the conformation of supracolloidal chains can be explained by the worm-like chain model. It is worthwhile to note that the R_g and R_e of some chains with contour lengths longer than 2,000 nm (solid circles in Figure 3.5) are located above the lines predicted by the worm-like chain model because these chains were apparently stretched as shown in the SEM images (Figure 3.6) possibly by spin-coating.

A self-supporting film consisting purely of semi-flexible supracolloidal chains can be produced if chains with long contour lengths are stacked with sufficient contact for mechanical stability. To deliver enough

chains for constructing a film, the spin-coating process was repeated instead of increasing the concentration of the solution because a high concentration of chains resulted in undesirable precipitation. As shown in Figure 3.7, more cycles of spin-coating delivered more chains on the substrate. Accordingly, more overlaps between the chains were also created. Successive overlaps of stacked chains are distinguishable in a side-view image (inset of Figure 3.7a), where red, green, blue, and yellow chains are sequentially coated. After 50 repeats of spin-coating (Figure 3.7c), most chains seemingly touched each other so that it is attempted to detach these chains as a whole film from the substrate by floating them on water as described in the experimental section. However, it wasn’t able to perceive a film on the water surface although delamination was verified by an image of the empty substrate after the detachment procedure.

According to an image of supracolloidal chains delivered by 100 cycles of spin-coating (Figure 3.8a), in which dense chains with abundant overlaps are visible, tolerable stability of the chains for detachment was expected. However, it was failed to fish a film out of the water surface, even though a film of the chains was briefly visible during detachment. After 200 cycles of spin-coating, a film of the chains floating on the water was able to be scooped and transferred onto another substrate, although the image of the chains was not much different from that after 100 cycles (Figure 3.8). The

inset in Figure 3.8b is a photograph of a transferred film of the chains (indicated by the arrow), implying the successful fabrication of a self-supporting film consisting solely of colloidal chains with mechanical stability enough for the transfer process, presumably originated from van der Waals interactions between the overlapping chains.

A film of supracolloidal chains after 100 or 200 repeats of spin-coating has a macroscopically continuous feature but has a lot of microscopic pores as shown in Figure 3.8 due to incomplete space-filling with semi-flexible colloidal chains. To estimate the average size of the pores, the high-resolution images of Figure 3.8a and 3.8b were digitized and displayed in Figures 3.8c and 3.8d, respectively. From the black spots, which are not covered by the chains, in the digitized images, the average pore diameters after 100 and 200 cycles of spin-coating are 42 nm and 37 nm, respectively, with the assumption of circular pores. This evaluation indicates the formation of nanoscale pores with potential control of their sizes by number of repeats of spin-coating. It is worthwhile to note that a porous film with a colloidal nature is unusual because colloids tend to form dense packing. Making semi-flexible chains with colloids can be a promising strategy to achieve a porous self-supporting colloidal film with a controllable pore size, which could find potential applications in size-selective membranes for nano-objects including viruses and catalytic filters after loading various catalysts in the colloids.

3.4. Conclusions

Supracolloidal chains polymerized from patchy micelles of PS-*b*-P4VP diblock copolymers were directly visualized in SEM images, from which persistence and contour lengths were effectively measured for conformational analysis. According to the evaluation, the supracolloidal chains were polymerized via the step-growth mechanism and showed semi-flexible nature so that their conformations were suitably explained by the worm-like chain model. In addition, a self-supporting film consisting purely of semi-flexible supracolloidal chains was produced because chains with long contour lengths were stacked each other with sufficient contacts for mechanical stability by spin-coating. Furthermore, the film had microscopic pores owing to incomplete space-filling with the semi-flexible colloidal chains. Since colloidal particles tend to form dense packing, a porous film essentially from colloidal constituents would not be easily achievable if there was no prior organization of them into a semi-flexible chain, which can open an opportunity for membrane applications of colloidal chains.

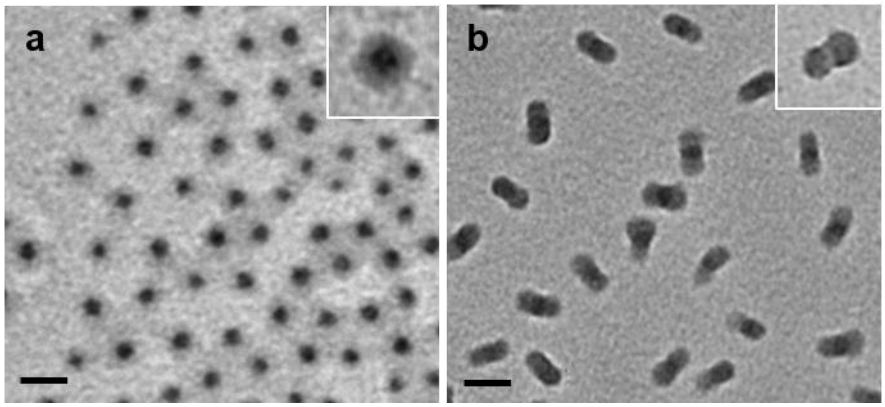

Figure 3.1 TEM images of PS(51)-*b*-P4VP(18) micelles after staining with I_2: (a) spherical micelles; (b) patchy micelles. The scale bars are 100 nm. The inset in (a) and (b) shows an enlarged image (100 nm × 100 nm) of individual spherical and patchy micelles, where the PS corona was stained with RuO_4, respectively.

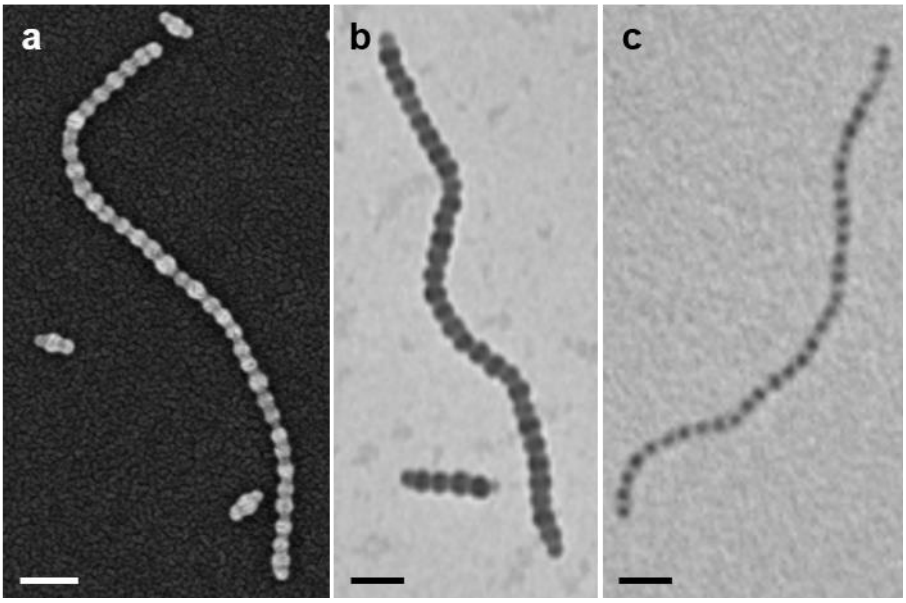

Figure 3.2 Supracolloidal chains of PS(51)-*b*-P4VP(18): (a) SEM image; (b) TEM image after staining the PS corona with RuO_4; (c) TEM image after staining the P4VP core with I_2. All scale bars in images are 100 nm.

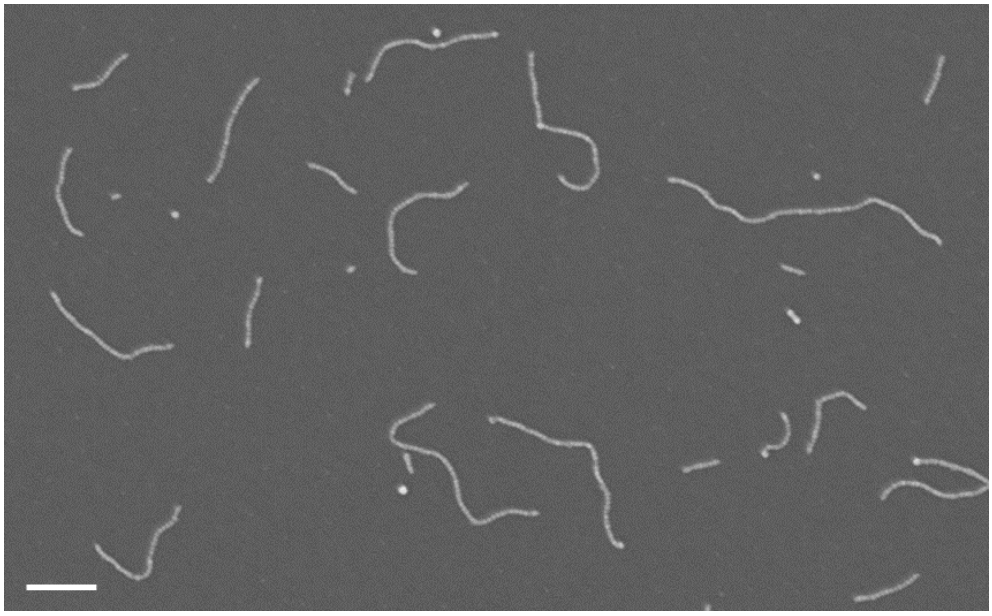

Figure 3.3 SEM image of supracolloidal chains spin-coated on a substrate. The scale bar is 500 nm.

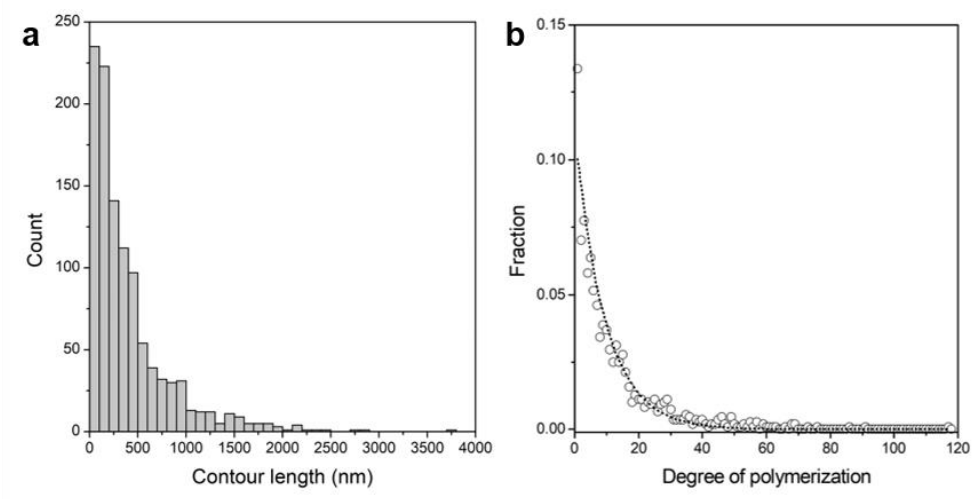

Figure 3.4 Size distributions of supracolloidal chains: (a) contour length; (b) degree of polymerization. The dotted line in (b) corresponds to a most-probable distribution in step-growth polymerization.

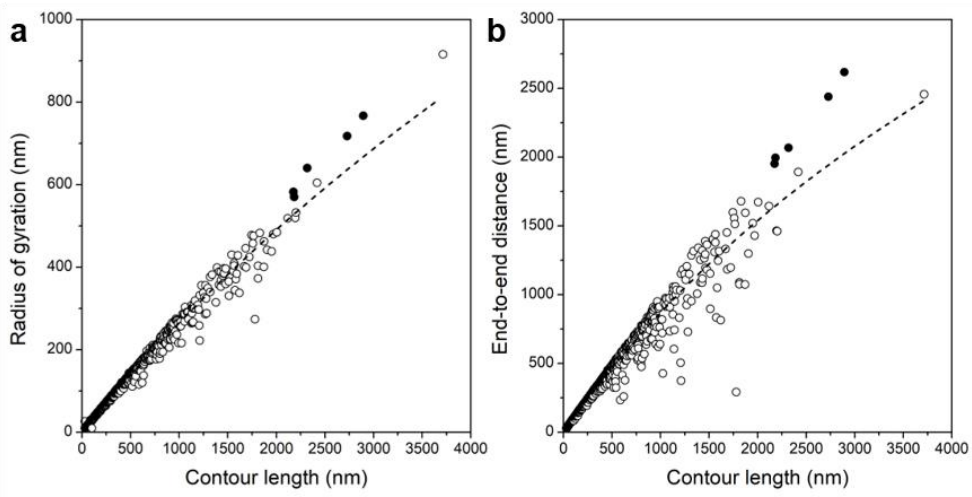

Figure 3.5 Semi-flexible supracollodial chains: (a) R_g vs. L; (b) R_e vs. L. The dashed lines in (a) and (b) are calculated by Equations 3.2 and 3.3 of the worm-like chain model, respectively.

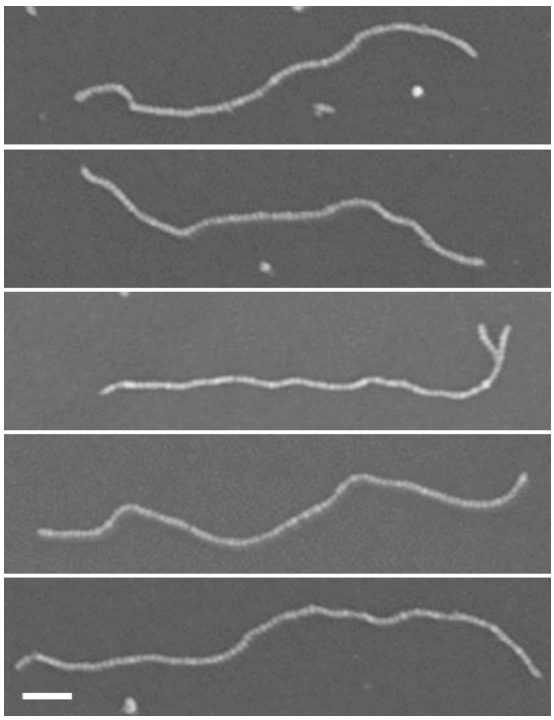

Figure 3.6 SEM images of supracolloidal chains marked with solid circles in Figure 3.5. They are displayed in order of contour lengths. The scale bar is 250 nm.

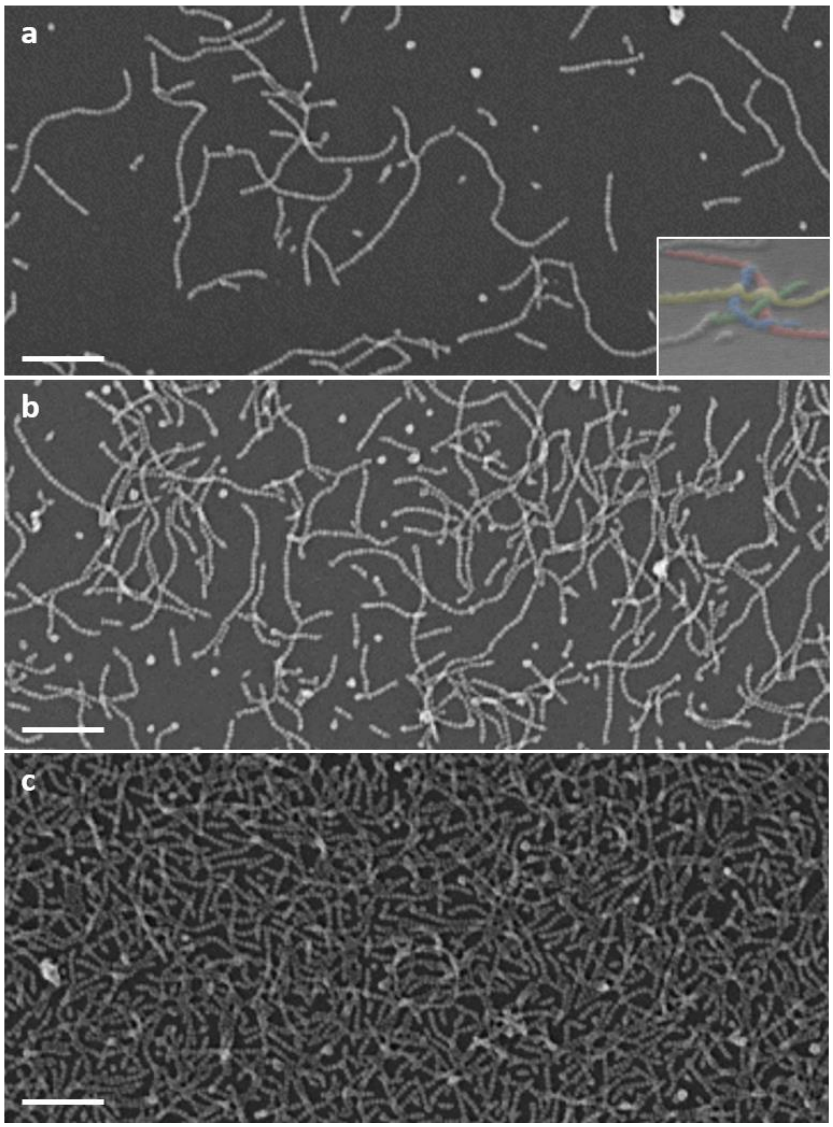

Figure 3.7 SEM images of supracolloidal chains on a substrate after repetitive spin-coating: (a) 5 cycles; (b) 20 cycles; (c) 50 cycles. The scale bars are 500 nm. The bottom inset in (a) is a side-view image in 500 nm × 400 nm, where chains are painted with false colors.

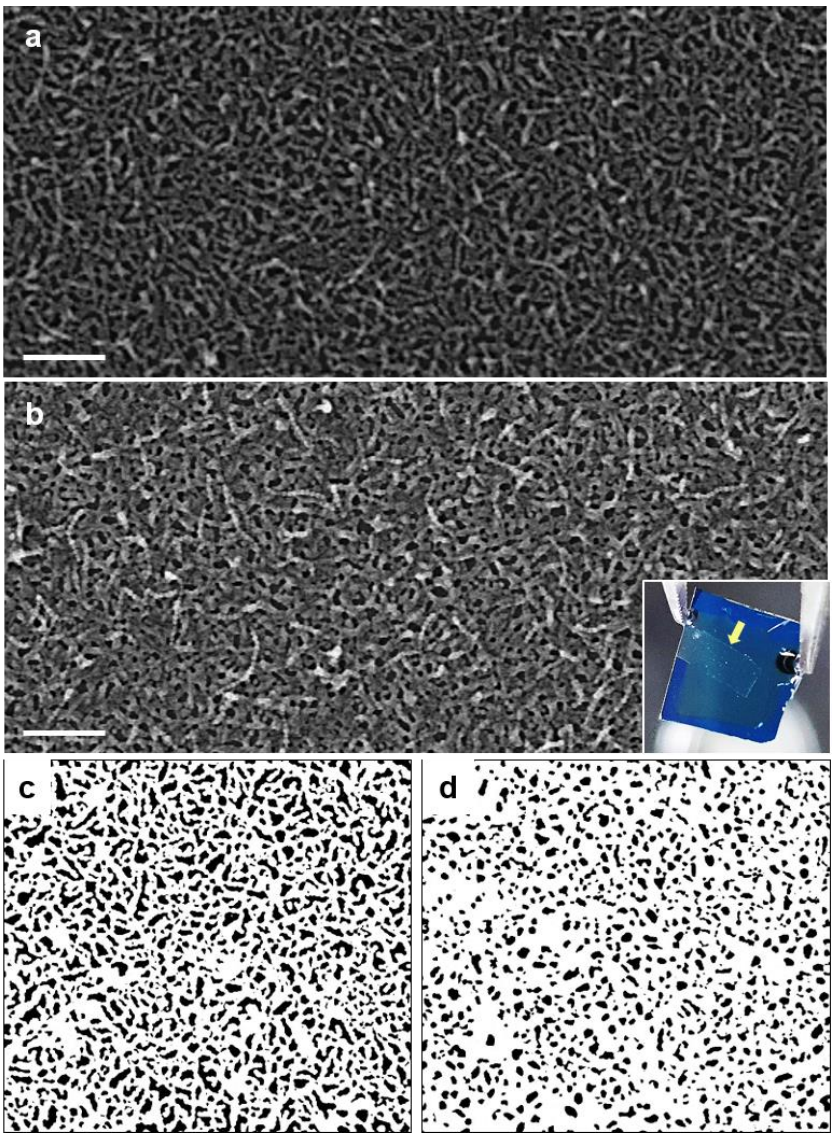

Figure 3.8 SEM images of supracolloidal chains on a substrate after repetitive spin-coating: (a) 100 cycles; (b) 200 cycles. The scale bars are 500 nm. The digitized images in (c) and (d) show black spots which are not covered by the chains from the high-resolution images corresponding to (a) and (b), respectively. The bottom inset in (b) shows a photograph of the film (indicated by the arrow) transferred onto a silicon wafer.

Chapter 4. PS−*b*−P4VP micelles incorporating cobalt nanoparticles as building blocks for supracolloidal chains

4.1. Introduction

As colloidal monomers of supracolloidal chains, a variety of inorganic nanoparticles have been reported to polymerize into a supracolloidal chain with novel properties [105,119,194]. In this process, the nanoparticles work as functional monomers of supracolloidal chains, which deliver their intrinsic properties to supracolloidal chains for various applications [105,119,194]. For example, supracolloidal chains of gold nanoparticles show catalytic activities for hydrogenation reaction [209], and supracolloidal chains of upconversion nanoparticles exhibit upconversion luminescence [210].

Block copolymer micelles can be utilized as an effective platform for assembling inorganic nanoparticles into supracolloidal chains. Because the chemical environment of micellar cores is distinct from that of corona, various functional nanoparticles such as plasmonic nanoparticles and quantum dots can be selectively loaded into the cores [211,212]. The block copolymer micelles functionalized with nanoparticles can then assemble into supracolloidal chains by inducing patches on their corona without affecting the nanoparticles embedded in micellar cores [170,174,175].

In this study, PS-*b*-P4VP micelles incorporating cobalt nanoparticles (CoNPs) are demonstrated as colloidal monomers of supracolloidal chains (Figure 4.1). By encapsulating cobalt nanoparticles with PS-*b*-P4VP,

spherical micelles consisting of cobalt nanoparticles–P4VP shell–PS corona are obtained. Then, the spherical micelles transform into patchy micelles via segregation of PS corona, after crosslinking P4VP shells. Finally, the patchy micelles polymerize into supracolloidal chains by adding water.

4.2. Experimental Section

Materials: Polystyrene-*b*-poly(4-vinylpyridine), PS(51)-*b*-P4VP(18), was purchased from Polymer Source, Inc. The numbers in the parenthesis are the number average molecular weights (M_n) in kg mol^{-1} and the polydispersity index (PDI) is 1.15. Trioctylphosphine oxide (TOPO) (99%), caffeic acid (98%), 1,2-dichlorobenzene (99%), iodomethane (99%), and 1,4-dibromobutane (99%) were purchased from Sigma-Aldrich. $Co_2(CO)_8$ (95%) and ethanol (96%) were obtained from Acros Organics. Oleic acid (99%) was purchased from TCI Chemicals. Commercially available solvents and chemicals were used as received.

Synthesis of cobalt nanoparticles: CoNPs were synthesized using the thermal decomposition method described in the literature [29]. TOPO (0.1 g) and oleic acid (0.2 ml) were dissolved in 1,2-dichlorobenzene (15 ml). The resulting solution was poured into a three-neck flask and purged with argon for 10 minutes. The solution was further flushed with argon for 30 minutes at 110 °C

and heated to 178 °C. Next, a solution of $Co_2(CO)_8$ (0.52 g) in 1,2-dichlorobenzene (3 ml) was rapidly injected into the refluxing bath. After stirring at 130 °C for 1 h and subsequent cooling cooled down to room temperature, the mixture solution was diluted with toluene (12 ml) and poured into ethanol (30 ml) to precipitate the particles. The precipitate was dispersed in $CHCl_3$. CoNPs were purified by collecting them with a permanent magnet and re-dispersed in $CHCl_3$.

Crosslinked PS-b-P4VP micelles with cobalt nanoparticles: PS-*b*-P4VP (5 mg) and cobalt nanoparticles (4 mg) were dissolved in chloroform (7 ml). After the addition of caffeic acid (2 mg), the solution was shaken at 35 °C for 12 h. Toluene (4.0 g) was slowly added to this mixture using a syringe pump at a rate of 4.0 ml/h to induce the formation of micelles. After mixing, chloroform was evaporated under reduced pressure and toluene was added to yield a 0.1 wt% solution of PS-*b*-P4VP micelles incorporating CoNPs. To crosslink the P4VP shells, 1,4-dibromobutane (DBB) (0.5 molar ratio to 4VP) was added to this solution, followed by shaking at 50 °C for 48 h. For linear assembly, the solution of crosslinked micelles was treated with iodomethane (2.0 molar ratio to 4VP) and shaken at 50 °C for 12 h to quaternize the P4VP shells.

Preparation of patchy micelles and supracolloidal chains: To produce colloidal monomers of patchy micelles, DMF (0.9 g) was added to a 0.1 wt% toluene solution of core-crosslinked micelles (0.1 g), resulting in a 0.01 wt% solution of patchy micelles. To polymerize the patchy micelles into supracolloidal chains, a mixture of deionized water and DMF (2.5:7.5 w/w) was added to a solution of patchy micelles to yield 12.5 wt% water in the final solution. The solution was kept at 30 °C without being stirred for 6 h.

Characterizations: Transmission electron microscopy (TEM) was performed using a Hitsachi H-7600 at 100 kV. TEM samples were prepared by dropping a solution of micelles or chains onto the TEM grid, with the excess solvent removed by using a filter paper and drying in the air. The TEM samples were exposed to I_2 or RuO_4 vapor to stain P4VP or PS, respectively. To study the magnetic behavior, solutions of each particle were dropped onto a TEM grid positioned between two permanent magnets. The strength of the magnetic field was 40 mT. CoNPs and spherical micelles were diluted with 1,2-dichlorobenzene and toluene to yield 0.01 wt% solutions, respectively. The solutions of patchy micelles and supracolloidal chains were cast without dilution.

4.3. Results and Discussion

As colloidal monomers of supracolloidal chains, micelles incorporating CoNPs were prepared by using an *ex-situ* encapsulation strategy. For the encapsulation, CoNPs were first synthesized by the thermal decomposition of cobalt precursors, as reported in the literatures [29,213]. Figure 4.2a shows the TEM image of as-prepared spherical CoNPs. The nanoparticles are highly monodispersed, and their average diameter is ~11 nm, as can be confirmed from the histogram shown in Figure 4.2b. It is noted that the CoNPs in Figure 4.2a are densely packed in a hexagonal array because they are coated with the ligands of small molecules [29,213].

These CoNPs were encapsulated with PS(51)-*b*-P4VP(18) copolymers, whose micelles assembled into linear supracolloidal chains [166]. CoNPs were first dispersed in a solution of PS-*b*-P4VP in chloroform, which is a good solvent for the CoNPs and two blocks of PS-*b*-P4VP. Caffeic acid was added to this solution in order to selectively ligate the P4VP blocks and CoNPs. Owing to the presence of carboxylic acid and catechol moieties, caffeic acid can ligate P4VP to the surface of CoNPs via hydrogen bonding with P4VP and binding to the metallic surface [214,215]. Next, toluene, a preferential solvent to PS, was added to the solution. By evaporating chloroform, a toluene solution of PS-*b*-P4VP micelles incorporating CoNPs was obtained.

The TEM image in Figure 4.3 shows the spherical micelles of PS-*b*-P4VP incorporating CoNPs. Dark CoNPs surrounded by polymeric shells are scattered across the entire field of view. In contrast to the as-prepared CoNPs shown in Figure 4.2, the CoNPs are not densely packed due to the thick polymeric shells. In the enlarged image shown in the bottom right inset, a PS corona appears as a dark sphere due to RuO_4 staining. In addition, a thin gray shell at the periphery of a CoNP is clearly visible even without staining, implying the P4VP shell directly attached to the particle. These observations indicate the core–shell–corona structure of micelles, which are composed of a CoNP core, P4VP shell, and PS corona. The diameter of the entire micelle, including the PS corona, is ~60 nm, which is slightly larger than that of pristine PS-*b*-P4VP micelles in toluene (~50 nm). It is noted that empty micelles of PS-*b*-P4VP, which appear as gray spheres without CoNPs, are also observed in Figure 2.3a. By counting the number of CoNPs in a single micelle, most micelles incorporate one CoNP (~86 %), while ~10% of micelles are empty, as evidenced by the histogram in Figure 4.3b. In addition, a small proportion of micelles had two or more CoNPs in their cores.

Pristine spherical micelles of PS-*b*-P4VP can transform into patchy micelles by adding DMF after crosslinking the cores [166,187]. Hence, the same protocol was applied to convert the micelles incorporating CoNPs into patchy micelles. First, the P4VP shells of spherical micelles were crosslinked with

1,4-dibromobutane. Next, DMF, which prefers P4VP to PS, was added to the solution. Upon the addition of DMF, the spherical micelles transformed into patchy micelles via the segregation of the PS corona, leading to the P4VP shell exposed to the solvent. Figure 4.4a shows the TEM images of the patchy micelles of PS-*b*-P4VP incorporating CoNPs. As shown in the upper image, bloated patches were induced on the surface of micelles without deterioration of the central CoNPs. After staining with RuO_4, the patches appear dark (bottom image), which can be clearly distinguished from the exposed P4VP shells surrounding the CoNPs. Each patchy micelle has two or three patches. In particular, ~69% of the patchy micelles have two patches, while ~31 % of them have three patches, as shown in Figure 4.4b. The proportion of the three-patch micelles is higher than that of the pristine micelles of PS(51)-*b*-P4VP(18) (~2 %), presumably originating from the reduced mobility of the P4VP block by strong interaction with CoNPs. With the assumption of spherical patches, the diameter of the patches was ~35 nm for two-patch micelles, which is slightly larger than those of the pristine micelles (~32 nm). In the case of three-patch micelles, the diameter of patches was ~28 nm.

By adding water, patchy micelles of PS(51)-*b*-P4VP(18) assemble into supracolloidal chains by merging non-polar PS patches to reduce unfavorable contact with water [166,187]. In this process, the exposed P4VP prevent lateral aggregation since they are still soluble to the solvent [166]. Accordingly, water was added to the solution of patchy micelles

incorporating CoNPs to induce linear assembly. However, all the patchy micelles rapidly precipitated rather than forming supracolloidal chains, implying insufficient repulsion between the exposed P4VP shells. The micelles, therefore, were treated with iodomethane (CH_3I) to increase lateral repulsive forces during the assembly. CH_3I quaternize the P4VP shells surrounding CoNPs, yielding $P(CH_34VP^+)I^-$, which can provide additional charges to the P4VP shells [216]. These micelles also transformed into patchy micelles in DMF, and successfully assembled into supracolloidal chains without noticeable precipitation, after adding water.

The TEM image of Figure 4.5 shows the supracolloidal chains assembled from PS-*b*-P4VP micelles incorporating CoNPs. Along a chain, dark CoNPs are connected through the merged patches, which appear gray lines between the CoNPs. Empty micellar cores, which look gray sphere, and those with two CoNPs are also observed because of the distribution of the number of CoNPs in a micelle (Figure 4.2b). It is noted that several chains are aggregated in a lateral and random fashion, implying relatively weak lateral repulsion to pristine PS-*b*-P4VP micelles. Importantly, encapsulating nanoparticles with PS-*b*-P4VP copolymers is a promising strategy to prepare colloidal monomers of supracolloidal chains, which are functionalized with nanoparticles.

Lastly, magnetic behaviors of micelles were investigated because CoNPs are the well-known magnetic nanoparticles. First, Figure 4.6a shows

the as-prepared CoNPs, which are drop-casted onto a TEM grid in the presence of an external magnetic field. The CoNPs formed microscopic fibers the CoNPs aligned in the direction of the magnetic field owing to their magnetic dipoles. Notably, after dried under the identical magnetic field, spherical micelles incorporating CoNPs left elongated blots aligned parallel to the field, as shown in the TEM images in Figure 4.6b. In addition, patchy micelles formed micro-sized fibers along the direction of the magnetic field (the TEM images of Figure 4.6c). The alignments imply that the magnetic dipoles of CoNPs are preserved during encapsulation and patch formation. It is noted that the fibers in Figure 4.6c are composed of small chunks, indicating that the patchy micelles first aggregate into small chunks during drying process, which subsequently aligned with the field. However, supracolloidal chains showed no evidence of alignment as shown in the TEM image of Figure 4.7. This observation could be understood by the magnetic nanoparticles positioned too far away in the rigid chains or low solution concentrations.

4.4. Conclusion

Spherical micelles of PS-*b*-P4VP incorporating CoNPs were obtained from the *ex-situ* encapsulation of CoNPs. The micelles were composed of a CoNP core, P4VP shell, and PS corona. After crosslinking the P4VP shells and changing the solvent to DMF, the spherical micelles transformed into patchy micelles via the segregation of PS corona. For linear assembly, the P4VP shells by quaternization to prevent lateral aggregation. The patchy micelles finally assembled into supracolloidal chains upon the addition of water. Importantly, encapsulating nanoparticles with PS-*b*-P4VP copolymers is a promising strategy to prepare colloidal monomers of supracolloidal chains, which are functionalized with nanoparticles. In the presence of an external magnetic field, spherical and patchy micelles aligned parallel to the direction of field, but supracolloidal chains showed no evidence of alignment.

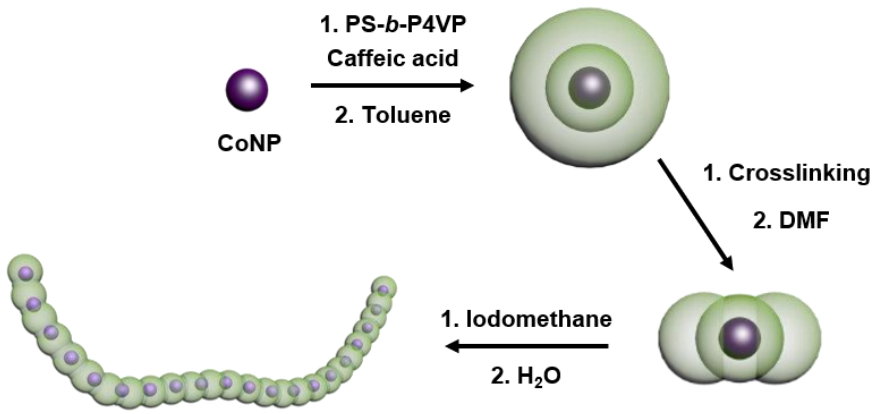

Figure 4.1 Schematic illustration of linear assembly of supracolloidal chains by using PS-*b*-P4VP micelles incorporating CoNPs as colloidal monomers.

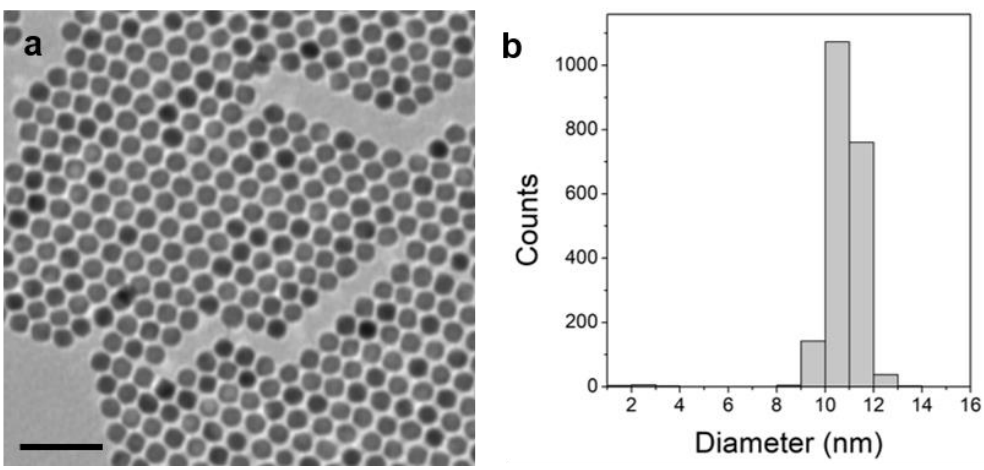

Figure 4.2 Cobalt nanoparticles (CoNPs): (a) TEM image; (b) Histogram showing the diameters of CoNPs. The scale bar is 50 nm.

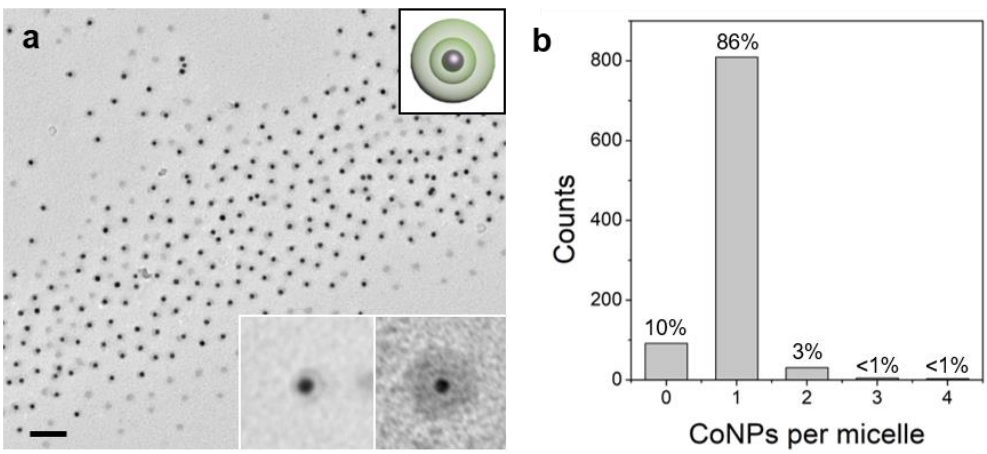

Figure 4.3 Spherical micelles of PS-*b*-P4VP incorporating CoNPs: (a) TEM image; (b) Histogram of the number of CoNPs in a micelle. The scale bar is 200 nm. The bottom insets show enlarged TEM images of spherical micelles in 100 × 100 nm. The TEM image in the right inset is obtained after staining PS with RuO_4. Schematic illustration is depicted in the upper inset.

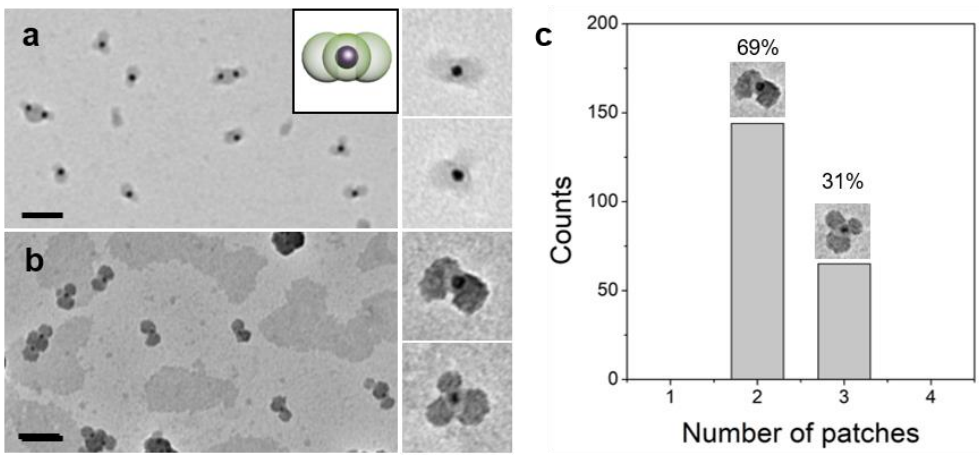

Figure 4.4 Patchy micelles of PS-*b*-P4VP incorporating CoNPs: (a) TEM images; (b) TEM images after staining with RuO_4; (c) Histogram of the number of patches. The scale bars are 100 nm. The insets show enlarged TEM images of patchy micelles in 100 × 100 nm. Schematic illustration is depicted in the inset of (a).

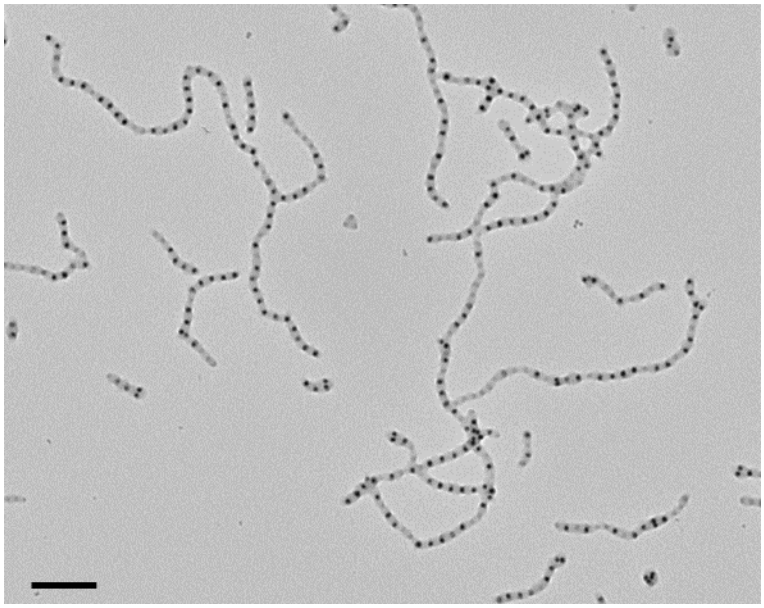

Figure 4.5 TEM image of supracolloidal chains of PS-*b*-P4VP incorporating cobalt nanoparticles. The scale bar is 200 nm.

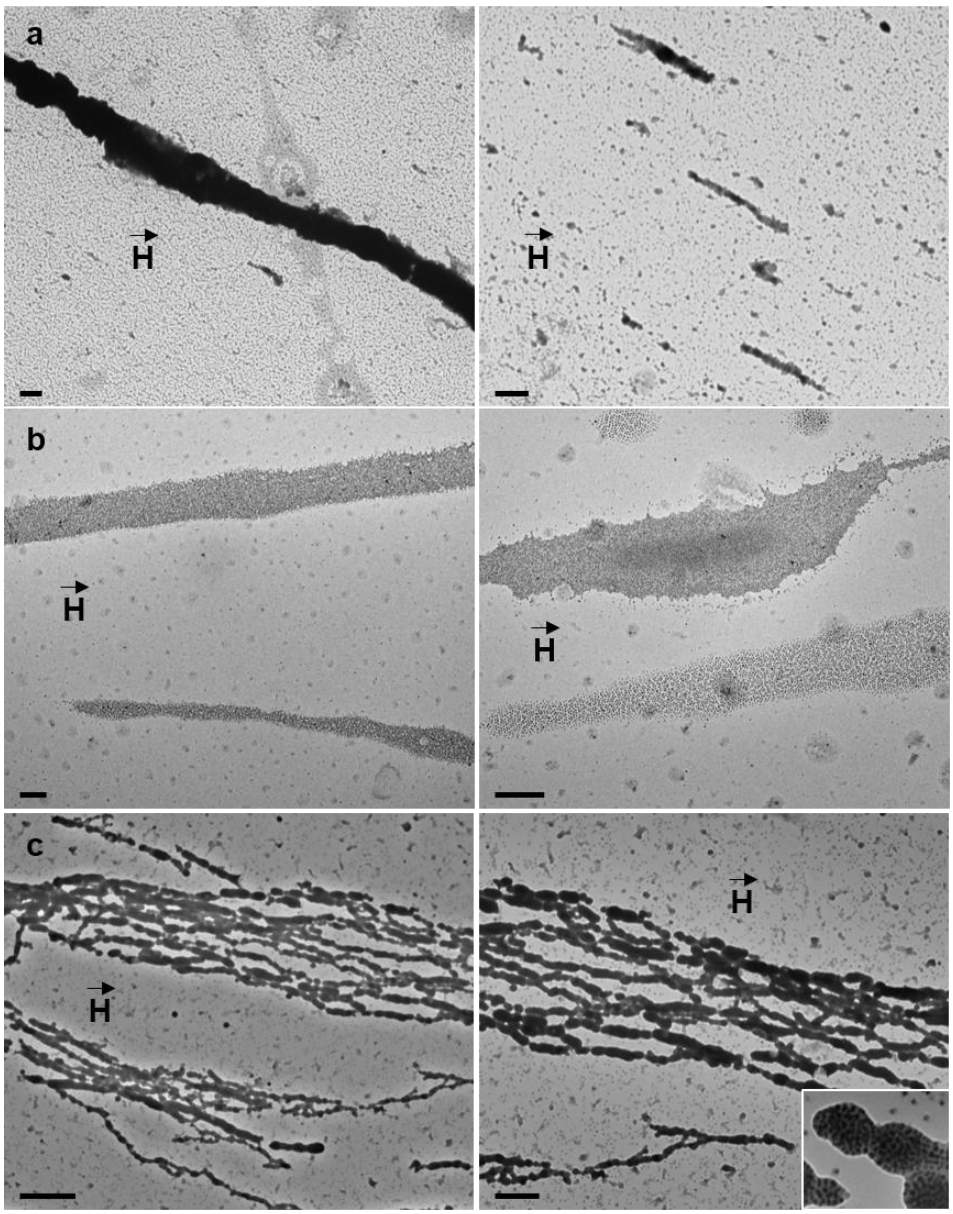

Figure 4.6 TEM images of CoNPs and micelles incorporating CoNPs after dried in the presence of a magnetic field: (a) CoNPs; (b) spherical micelles; (c) patchy micelles. The scale bars are 1 μm. The inset in (c) shows the magnified image in 500 nm × 400 nm.

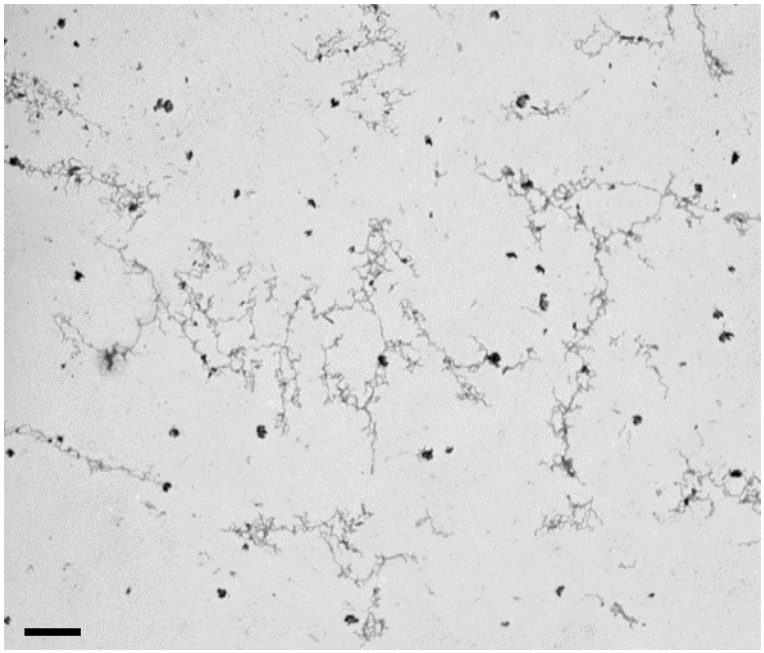

Figure 4.7 TEM image of supracolloidal chains incorporating CoNPs after dried in the presence of a magnetic field. The scale bar is 2 μm.

Bibliography

[1] V. Iablokov, S. K. Beaumont, S. Alayoglu, V. V. Pushkarev, C. Specht, J. Gao, A. P. Alivisatos, N. Kruse, G. A. Somorjai, *Nano Lett.* **2012**, 12, 6, 3091.

[2] I. T. Papadas, I. Vamvasakis, I. Tamiolakis, G. S. Armatas, *Chem. Mater.* **2016**, 28, 9, 2886.

[3] S. S. Kim, B. H. Sohn, *Carbon*, **2016**, 107, 124.

[4] G. Kaptay, *Int. J. Pharm.* **2012**, 430, 1, 253.

[5] T. Cowen, K. Karim, S. A. Piletsky, *Polym. Chem.* **2018**, 9, 4566.

[6] H. Wang, D. W. Brandl, P. Nordlander, N. J. Halas, *Acc. Chem. Res.* **2007**, 40, 1, 53.

[7] L. Amidani, T. V. Plakhova, A. Y. Romanchuk, E. Gerber, S. Weiss, A. Efimenko, C. J. Sahle, S. M. Butorin, S. N. Kalmykov, K. O. Kvashnina, *Phys. Chem. Chem. Phys*. **2019**, 21, 10635.

[8] S. Jun, J. Lee, E. Jang, *ACS Nano*, **2013**, *7*, 2, 1472.

[9] F. P. García de Arquer, D. V. Talapin, V. I. Klimov, Y. Arakawa, M. Bayer, E. H. Sargent, *Science*, **2021**, 373, 6555, eaaz8541.

[10] C. R. Kagan, L. C. Bassett, C. B. Murray, S. M. Thompson, *Chem. Rev.* **2021**, 121, 5, 3186.

[11] K. A. Willets, R. P. van Duyne, *Annu. Rev. Phys. Chem.* **2007**, 58, 267.

[12] J. Jana, M. Ganguly, T. Pal, *RSC Adv*. **2016**, 6, 86174.

[13] C. P. Bean, J. D. Livingston, *J. Appl. Phys.* **1959**, 30, S120.

[14] S. Bedanta, W. Kleemann, *J. Phys. D: Appl. Phys.* **2009**, 42, 013001.

[15] H. Moustaoui, J. Saber, I. Djeddi, Q. Liu, A. T. Diallo, J. Spadavecchia, M. Lamy De La Chapelle, N. Djaker, *J. Phys. Chem. C.* **2019**, 123, 28, 17548.

[16] M. Kim, J. H. Lee, J. M. Nam, *Adv. Sci.* **2019**, 6, 1900471.

[17] A. H. Lu, E. L. Salabas, F. Schüth, *Angew. Chem. Int. Ed.* **2007**, 46, 1222.

[18] C. B. Murray, S. Sun, H. Doyle, T. Betley, *MRS Bulletin,* **2001**, 26, 985.

[19] T. Trindade, P. O'Brien, N. L. Pickett, *Chem. Mater.* **2001**, 13, 11, 3843.

[20] N. Lee, T. Hyeon, *Chem. Soc. Rev.* **2012**, 41, 2575.

[21] P. Reiss, M. Protiere, L. Li, *Small* **2009**, 5, 2, 154.

[22] S. S. Narender, V. Venkata. S. Varma, C. S. Srikar, J. Ruchitha, P. A. Varma, B. V. S. Praveen, *Chem Eng Technol* **2022**, 45, 3, 397.

[23] A. V. Nikam, B. L. V. Prasad, A. A. Kulkarni, *CrystEngComm* **2018**, 20, 5091.

[24] Y. Mai, A. Eisenberg, *Chem. Soc. Rev.* **2012**, 41, 5969.

[25] K. H. Ku, J. M. Shin, H. Yun, G. R. Yi, S. G. Jang, B. J. Kim, *Adv. Funct. Mater.* **2018**, 28, 1802961.

[26] M. Karayianni, S. Pispas, *J. Polym. Sci.* **2021**, 59, 1874.

[27] C. van der Wel, R. K. Bhan, R. W. Verweij, H. C. Frijters, Z. Gong, A. D. Hollingsworth, S. Sacanna, D. J. Kraft, *Langmuir*, **2017**, 33, 33, 8174.

[28] S. Huang, Z. Li, L. Kong, N. Zhu, A. Shan, L. Li, *J. Am. Chem. Soc.* **2016**, 138, 18, 5749.

[29] V. F. Puntes, K. M. Krishnan, A. P. Alivisatos, *Science*, **2001**, 291, 5511, 2115.

[30] J. Park, J. Joo, G. K. Soon, Y. Jang, T. Hyeon, *Angew. Chem. Int. Ed.* **2007**, 46, 4630.

[31] J. Muro-Cruces, A. G. Roca, A. López-Ortega, E. Fantechi, D. Del-Pozo-Bueno, S. Estradé, F. Peiró, B. Sepúlveda, F. Pineider, C. Sangregorio, J. Nogues, *ACS Nano* **2019,** 13, 7, 7716.

[32] B. Gao, G. Arya, A. R. Tao, *Nat. Nanotechnol.* **2012**, 7, 433.

[33] H. Chen, L. Shao, Q. Li, J. Wang, *Chem. Soc. Rev.* **2013**, *42*, 2679.

[34] S. E. Lohse, C. J. Murphy, *Chem. Mater.* **2013**, 25, 8, 1250.

[35] J. Kim, Z. Ou, M. R. Jones, X. Song, Q. Chen, *Nat Commun.* **2017**, 8, 761.

[36] A. Kim, S. Zhou, L. Yao, S. Ni, B. Luo, C. E. Sing, Q. Chen, *J. Am. Chem. Soc.* **2019**, 141, 30, 11796.

[37] X. Chen, D. Peng, Q. Ju, F. Wang, *Chem. Soc. Rev.* **2015**, 44, 1318.

[38] N. X. V. Lan, J. Moon, T. H. Kang, K. Wang, H. G. Park, G. R. Yi, *Chem. Mater.* **2021**, 33, 5, 1714.

[39] R. G. Chaudhuri, S. Paria, *Chem. Rev.* **2012**, 112, 4, 2373.

[40] Q. Luo, Z. Shi, Y. Zhang, X. J. Chen, S. Y. Han, T. Baumgart, D. M. Chenoweth, S. J. Park, *J. Am. Chem. Soc.* **2016**, 138, 32, 10157.

[41] Y. Sun, F. Gao, Y. Yao, H. Jin, X. Li, S. Lin, *ACS Macro Lett.* **2021**, 10, 5, 525.

[42] M. Niederberger, *Adv. Funct. Mater.* **2017**, 27, 1703647.

[43] F. Li, D. P. Josephson, A. Stein, *Angew. Chem. Int. Ed.* **2011**,50, 360.

[44] M. A. Boles, M. Engel, D. V. Talapin, *Chem. Rev.* **2016**, 116, 18, 11220.

[45] X. Bouju, É. Duguet, F. Gauffre, C. R. Henry, M. L. Kahn, P. Mélinon, S. Ravaine, *Adv. Mater.* **2018**, 30, 1706558.

[46] J. Liu, J. Huang, W. Niu, C. Tan, H. Zhang, *Chem. Rev.* **2021**, 121, 10, 5830.

[47] T. Ming, X. Kou, H. Chen, T. Wang, H. L. Tam, K. W. Cheah, J. Y. Chen, J. Wang, *Angew. Chem. Int. Ed.* **2008**, 47, 9685.

[48] T. K. Sau, C. J. Murphy, *Langmuir*, **2005**, 21, 7, 2923.

[49] C. R. Laramy, H. Lopez-Rios, M. N. O'Brien, M. Girard, R. J. Stawicki, B. Lee, M. O. de La Cruz, C. A. Mirkin, *ACS Nano*, **2019**, 13, 2, 1412.

[50] P. J. Santos, P. A. Gabrys, L. Z. Zornberg, M. S. Lee, R. J. Macfarlane, *Nature*, **2021**, 591, 586.

[51] J. S. Oh, G. R. Yi, D. J. Pine, *ACS Nano*, **2020**, *14*, 11, 15786.

[52] M. He, J. P. Gales, É. Ducrot, Z. Gong, G. R. Yi, S. Sacanna, D. J. Pine, *Nature*, **2020**, 585, 524.

[53] A. Neophytou, V. N. Manoharan, D. Chakrabarti, *ACS Nano*, **2021**, 15, 2, 2668.

[54] M. B. Ross, J. C. Ku, V. M. Vaccarezza, G. C. Schatz, C. A. Mirkin, *Nat. Nanotechnol.* **2015**, 10, 453.

[55] C. R. Kagan, C. B. Murray, *Nat. Nanotechnol.* **2015**, 10, 1013.

[56] A. Courty, A. Mermet, P. A. Albouy, E. Duval, M. P. Pileni, *Nat. Mater.* **2005**, 4, 395.

[57] W. Walravens, J. D. Roo, E. Drijvers, S. ten Brinck, E. Solano, J. Dendooven, C. Detavernier, I. Infante, Z. Hens, *ACS Nano*, **2016**, *10*, 1163.

[58] T. Paik, B. T. Diroll, C. R. Kagan, C. B. Murray, *J. Am. Chem. Soc.* **2015**, 137, 20, 6662.

[59] Q. Chen, S. C. Bae, S. Granick, *Nature*, **2011**, 469, 381.

[60] J. Li, X. Liu, J. Jin, N. Yan, W. Jiang, *Nanotechnology* **2022**, 33, 38, 385601.

[61] H. Wang, L. Yao, X. Mao, K. Wang, L. Zhu, J. Zhu, *Nanoscale*, **2019**, 11, 13917.

[62] S. Wintzheimer, T. Granath, M. Oppmann, T. Kister, T. Thai, T. Kraus, N. Vogel, K. Mandel, *ACS Nano*, **2018**, 12, 6, 5093.

[63] Q. Y. Lin, J. A. Mason, Z. Li, W. Zhou, M. N. O'Brien, K. A. Brown, M. R. Jones, S. Butun, B. Lee, V. P. Dravid, K. Aydin, C. A. Mirkin,

Science, **2018**, 359, 669.

[64] V. Flauraud, M. Mastrangeli, G. D. Bernasconi, J. Butet, D. T. L. Alexander, E. Shahrabi, O. J. F. Martin, J. Brugger, *Nat. Nanotechnol.* **2017**, 12, 73.

[65] G. Chen, K. J. Gibson, D. Liu, H. C. Rees, J. H. Lee, W. Xia, R. Lin, H. L. Xin, O. Gang, Y. Weizmann, *Nat. Mater.* **2019**, *18*, 169.

[66] Y. J. Kim, J. bin Moon, H. Hwang, Y. S. Kim, G. R. Yi, *Adv. Mater.* **2022**, *2203045*.

[67] D. Morphew, D. Chakrabarti, *Curr. Opin. Colloid Interface Sci.* **2017**, 30, 70.

[68] É. Ducrot, M. He, G. R. Yi, D. J. Pine, *Nat. Mater.* **2017**, 16, 652.

[69] Z. Lu, Y. Yin, *Chem. Soc. Rev.* **2012**, 41, 6874.

[70] L. Shang, Y. Liang, M. Li, G. I. N. Waterhouse, P. Tang, D. Ma, L. Z. Wu, C. H. Tung, T. Zhang, *Adv. Funct. Mater.* **2017**, 27, 1606215.

[71] S. Singamaneni, V. N. Bliznyuk, C. Binek, E. Y. Tsymbal, *J. Mater. Chem.* **2011**, 21, 16819.

[72] M. Wang, L. He, Y. Yin, *Mater. Today,* **2013**, 16, 110.

[73] L. J. Hill, N. E. Richey, Y. Sung, P. T. Dirlam, J. J. Griebel, E. Lavoie-Higgins, I. B. Shim, N. Pinna, M. G. Willinger, W. Vogel, J. J. Benkoski, K. Char, J. Pyun, *ACS Nano*, **2014**, 8, 4, 3272.

[74] S. L. Tripp, S. V. Pusztay, A. E. Ribbe, A. Wei, *J. Am. Chem. Soc.* **2002**, 124, 7914.

[75] N. G. Pavlopoulos, J. T. Dubose, N. Pinna, M. G. Willinger, K. Char, J. Pyun, *Angew. Chem. Int. Ed.* **2016**, 55, 1787.

[76] J. Townsend, R. Burtovyy, Y. Galabura, I. Luzinov, *ACS Nano* **2014**, *8*, 7, 6970.

[77] L. Balcells, I. Stanković, Z. Konstantinović, A. Alagh, V. Fuentes, L. López-Mir, J. Oró, N. Mestres, C. García, A. Pomar, B. Martínez, *Nanoscale*, **2019**, 11, 14194.

[78] P. Dhak, M. K. Kim, J. H. Lee, M. Kim, S. K. Kim, *J. Magn. Magn. Mater.* **2017**, 433, 47.

[79] L. J. Hill, J. Pyun, *ACS Appl. Mater. Interfaces*, **2014**, 6, 9, 6022.

[80] P. Y. Keng, I. Shim, B. D. Korth, J. F. Douglas, J. Pyun, *ACS Nano* **2007**, 1, 4, 279.

[81] B. D. Korth, P. Keng, I. Shim, S. E. Bowles, C. Tang, T. Kowalewski, K. W. Nebesny, J. Pyun, *J. Am. Chem. Soc.* **2006**, 128, 20, 6562

[82] J. Byrom, P. Han, M. Savory, S. L. Biswal, *Langmuir*, **2014**, *30*, 30, 9045.

[83] B. Bharti, A. L. Fameau, M. Rubinstein, O. D. Velev, *Nat. Mater.* **2015**, 14, 1104.

[84] U. Jeong, X. Teng, Y. Wang, H. Yang, Y. Xia, *Adv. Mater.* **2007**, 19, 33.

[85] J. Faraudo, J. S. Andreu, C. Calero, J. Camacho, *Adv. Funct. Mater.* **2016**, 26, 3837.

[86] M. B. Bannwarth, S. Utech, S. Ebert, D. A. Weitz, D. Crespy, K.

Landfester, *ACS Nano,* **2015**, 9, 3, 2720.

[87] D. Li, S. Banon, S. L. Biswal, *Soft Matter,* **2010**, 6, 4197.

[88] D. Li, J. Rogers, S. L. Biswal, *Langmuir,* **2009**, 25, 16, 8944.

[89] Z. Tang, N. A. Kotov, M. Giersig, *Science,* **2002**, *297*, 237.

[90] G. D. Lilly, J. Lee, K. Sun, Z. Tang, K. S. Kim, N. A. Kotov, *J. Phys. Chem. C,* **2008**, 112, 2, 370.

[91] C. Yi, Y. Yang, Z. Nie, *J. Am. Chem. Soc.* **2019**, 141, 19, 7917.

[92] C. Yi, H. Liu, S. Zhang, Y. Yang, Y. Zhang, Z. Lu, E. Kumacheva, Z. Nie, *Science,* **2020**, 369, 1369.

[93] K. D. Hermanson, S. O. Lumsdon, J. P. Williams, E. W. Kaler, O. D. Velev, *Science,* **2001**, 294, 1082.

[94] K. Jathavedan, S. K. Bhat, P. S. Mohanty, *J. Colloid Interface Sci.* **2019**, 544, 88.

[95] B. Bharti, F. Kogler, C. K. Hall, S. H. L. Klapp, O. D. Velev, *Soft Matter,* **2016**, 12, 7747.

[96] B. Bharti, O. D. Velev, *Langmuir,* **2015**, 31, 29, 7897.

[97] J. J. Crassous, A. M. Mihut, E. Wernersson, P. Pfleiderer, J. Vermant, P. Linse, P. Schurtenberger, *Nat Commun* **2014**, 5, 5516.

[98] A. Ruditskiy, B. Ren, I. Kretzschmar, *Soft Matter* **2013**, 9, 9174.

[99] P. Song, Y. Wang, Y. Wang, A. D. Hollingsworth, M. Weck, D. J. Pine, M. D. Ward, *J. Am. Chem. Soc.* **2015**, 137, 8, 3069.

[100] S. Gangwal, A. Pawar, I. Kretzschmar, O. D. Velev, *Soft Matter* **2010**,

6, 1413.

[101] I. S. Jo, S. Lee, J. Zhu, T. S. Shim, G. R. Yi, *Curr. Opin. Colloid Interface Sci.* **2017**, 30, 97.

[102] J. Du, R. K. O'Reilly, *Chem Soc Rev* **2011**, *40*, 2402.

[103] S. Ravaine, E. Duguet, *Curr. Opin. Colloid Interface Sci.* **2017**, 30, 45.

[104] W. Li, H. Palis, R. Mérindol, J. Majimel, S. Ravaine, E. Duguet, *Chem. Soc. Rev.* **2020**, 49, 1955.

[105] X. Fan, A. Walther, *Chem. Soc. Rev.* **2022**, 51, 4023.

[106] E. Elacqua, X. Zheng, C. Shillingford, M. Liu, M. Weck, *Acc. Chem. Res.* **2017**, 50, 11, 2756.

[107] M. Gerth, I. K. Voets, *Chem. Commun.* **2017**, 53, 4414.

[108] Nonappa, O. Ikkala, *Adv. Funct. Mater.* **2018**, 28, 1704328.

[109] M. Zhai, Q. Chen, W. Yuan, Q. Shi, H. Xu, *Mater. Chem. Front.* **2019**, 3, 1888.

[110] Y. Wang, Y. Wang, D. R. Breed, V. N. Manoharan, L. Feng, A. D. Hollingsworth, M. Weck, D. J. Pine, *Nature*, **2012**, 491, 51.

[111] W. Liu, J. Halverson, Y. Tian, A. V. Tkachenko, O. Gang, *Nat. Chem.* **2016**, 8, 867.

[112] X. Zheng, Y. Wang, Y. Wang, D. J. Pine, M. Weck, *Chem. Mater.* **2016**, 28, 11, 3984.

[113] F. Benyettou, X. Zheng, E. Elacqua, Y. Wang, P. Dalvand, Z. Asfari,

J. C. Olsen, D. S. Han, N. Saleh, M. Elhabiri, M. Weck, A. Trabolsi, *Langmuir*, **2016**, 32, 28, 7144.

[114] K. Han, D. Go, D. Hoenders, A. J. C. Kuehne, A. Walther, *ACS Macro Lett.* **2017**, 6, 3, 310.

[115] Y. Wang, A. D. Hollingsworth, S. K. Yang, S. Patel, D. J. Pine, M. Weck, *J. Am. Chem. Soc.* **2013**, 135, 38, 14064.

[116] L. Chen, L. Lu, S. Wang, Y. Xia, *ACS Sens.* **2017**, 2, 6, 781.

[117] S. Zhang, X. Kou, Z. Yang, Q. Shi, G. D. Stucky, L. Sun, J. Wang, C. Yan, *Chem. Commun.* **2007**, 1816.

[118] Z. Nie, D. Fava, E. Kumacheva, S. Zou, G. C. Walker, M. Rubinstein, *Nat. Mater.* **2007**, *6, 609.*

[119] R. M. Choueiri, E. Galati, A. Klinkova, H. Thérien-Aubin, E. Kumacheva, *Faraday Discuss.* **2016**, 191, 189.

[120] S. K. Mehetor, H. Ghosh, N. Pradhan, *J. Phys. Chem. Lett.* **2019**, 10, 6, 1300.

[121] Y. Yang, Y. H. Lee, C. L. Lay, X. Y. Ling, *Chem. Mater.* **2017**, 29, 14, 6137.

[122] B. Liu, W. Li, E. Duguet, S. Ravaine, *ACS Macro Lett*. **2022**, 11, 1, 156.

[123] W. Li, B. Liu, C. Hubert, A. Perro, E. Duguet, S. Ravaine, *Nano Res.* **2020**, 13, 3371.

[124] H. Qiu, Z. M. Hudson, M. A. Winnik, I. Manners, *Science*, **2015**, 347, 6328, 1329.

[125] S. K. Ghosh, T. Pal, *Chem. Rev.* **2007**, 107, 11, 4797.

[126] G. Aguirregabiria, J. Aizpurua, R. Esteban, *Opt. Express.* **2017**, 25, 12, 13760.

[127] K. Liu, A. Lukach, K. Sugikawa, S. Chung, J. Vickery, H. Therien-Aubin, B. Yang, M. Rubinstein, E. Kumacheva, *Angew. Chem.* **2014**, 126, 2686.

[128] A. Klinkova, H. Thérien-Aubin, A. Ahmed, D. Nykypanchuk, R. M. Choueiri, B. Gagnon, A. Muntyanu, O. Gang, G. C. Walker, E. Kumacheva, *Nano Lett.* **2014**, 14, 11, 6314

[129] L. Chang, Y. Khan, L. Li, N. Yang, P. Yin, L. Guo, *RSC Adv.* **2017**, 7, 13896.

[130] K. Liu, A. Ahmed, S. Chung, K. Sugikawa, G. Wu, Z. Nie, R. Gordon, E. Kumacheva, *ACS Nano*, **2013**, 7, 7, 5901.

[131] Z. Ma, J. Mohapatra, K. Wei, J. P. Liu, S. Sun, *Chem, Rev.* **2021**, https://10.1021/acs.chemrev.1c00860.

[132] J. J. Benkoski, J. L. Breidenich, O. M. Uy, A. T. Hayes, R. M. Deacon, H. B. Land, J. M. Spicer, P. Y. Keng, J. Pyun, *J. Mater. Chem.* **2011**, 21, 7314.

[133] H. Inaba, M. Yamada, M. R. Rashid, A. M. R. Kabir, A. Kakugo, K. Sada, K. Matsuura, *Nano Lett.* **2020**, 20, 7, 5251.

[134] T. Yang, B. Sprinkle, Y. Guo, J. Qian, D. Hua, A. Donev, D. W. M. Marr, N. Wu, *Proc. Natl. Acad. Sci. U S.A.* **2020**, 117, 31, 18186.

[135] R. Uebe, D. Schüler, *Nat. Rev. Microbiol.* **2016**, 14, 621.

[136] J. F. Galisteo-López, M. Ibisate, R. Sapienza, L. S. Froufe-Pérez, Á. Blanco, C. López, *Adv.Mater.* **2011**, 23, 30.

[137] J. D. Joannopoulos, P. R. Villeneuve, S. Fan, *Nature*, **1997**, 386, 143.

[138] G. von Freymann, V. Kitaev, B. v. Lotsch, G. A. Ozin, *Chem. Soc. Rev.*, 2013, 42, 2528.

[139] K. Li, C. Li, H. Li, M. Li, Y. Song, *iScience* **2021**, 24, 2 102121.

[140] W. Luo, Q. Cui, K. Fang, K. Chen, H. Ma, J. Guan, *Nano Lett.* **2020**, 20, 2, 803.

[141] L. He, Y. Hu, X. Han, Y. Lu, Z. Lu, Y. Yin, *Langmuir*, **2011**, 27, 22, 13444.

[142] L. He, M. Wang, J. Ge, Y. Yin, *Acc. Chem. Res.* **2012**, 45, 9, 1431.

[143] J. Ge, H. Lee, L. He, J. Kim, Z. Lu, H. Kim, J. Goebl, S. Kwon, Y. Yin, *J. Am. Chem. Soc.* **2009**, 131, 43, 15687.

[144] M. Wang, L. He, Y. Hu, Y. Yin, *J. Mater. Chem. C*, **2013**, 1, 6151.

[145] M. C. Li, Q. Wu, R. J. Moon, M. A. Hubbe, M. J. Bortner, *Adv. Mater.* **2021**, 33, 2006052.

[146] M. Saitoh, Y. Kashiwagi, M. Chigane, *Soft Matter*, **2017**, 13, 3927.

[147] J. de Vicente, D. J. Klingenberg, R. Hidalgo-Alvarez, *Soft Matter* **2011**, 7, 3701.

[148] M. Ashtiani, S. H. Hashemabadi, A. Ghaffari, *J. Magn. Magn. Mater.* **2015**, 374, 716.

[149] Y. D. Liu, H. J. Choi, *Soft Matter* **2012**, 8, 11961.

[150] T. Hao, *Adv. Mater.* **2001**, 13, 24, 1847.

[151] I. Bica, Y. D. Liu, H. J. Choi, *J. Ind. Eng. Chem.* **2013**, 19, 2, 394.

[152] S. Yang, C. Cao, Y. Sun, P. Huang, F. Wei, W. Song, *Angew. Chem. Int. Ed.* **2015**, 54, 2661.

[153] W. H. Chong, L. K. Chin, R. L. S. Tan, H. Wang, A. Q. Liu, H. Chen, *Angew. Chem. Int. Ed*. **2013**, 52, 8570.

[154] R. Dreyfus, J. Baudry, M. L. Roper, M. Fermigier, H. A. Stone, J. Bibette, *Nature,* **2005**, 437, 862.

[155] T. P. Lodge, *Macromol. Chem. Phys*. **2003**, 20, 2, 265.

[156] C. M. Bates, F. S. Bates, *Macromolecules* **2017**, *50*, 1, 3.

[157] J. K. Kim, S. Y. Yang, Y. Lee, Y. Kim, *Prog. Polym. Sci.* **2010**, 35, 11, 1325.

[158] X. Qiang, R. Chakroun, N. Janoszka, A. H. Gröschel, *Isr. J. Chem.* **2019**, 59, 945.

[159] N. Hadjichristidis, H. Iatrou, M. Pitsikalis, S. Pispas, A. Avgeropoulos, *Prog. Polym. Sci.* **2005**, 30, 7, 725.

[160] C. Li, Q. Li, Y. V. Kaneti, D. Hou, Y. Yamauchi, Y. Mai, *Chem. Soc. Rev.* **2020**, 49, 4681.

[161] G. Riess, *Prog. Polym. Sci.* **2003**, 28, 7, 1107.

[162] A. Blanazs, S. P. Armes, A. J. Ryan, *Macromol. Rapid Commun.* **2009**, 30, 267.

[163] U. Tritschler, S. Pearce, J. Gwyther, G. R. Whittell, I. Manners,

Macromolecules, **2017**, 50, 9, 3439.

[164] Y. Lu, J. Lin, L. Wang, L. Zhang, C. Cai, *Chem. Rev.* **2020**, 120, 9, 4111.

[165] T. L. Nghiem, T. I. Löbling, A. H. Gröschel, *Polym Chem* **2018**, *9*, 1583.

[166] J. H. Kim, W. J. Kwon, B. H. Sohn, *Chem. Commun*. **2015**, 51, 3324.

[167] A. Walther, A. H. E. Müller, *Chem. Commun.* **2009**, 1127.

[168] D. J. Pochan, J. Zhu, K. Zhang, K. L. Wooley, C. Miesch, T. Emrick, *Soft Matter*, **2011**, 7, 2500.

[169] H. Gao, L. Gao, J. Lin, Y. Lu, L. Wang, C. Cai, X. Tian, *Macromolecules* **2020**, 53, 9, 3571.

[170] A. H. Gröschel, A. Walther, T. I. Löbling, F. H. Schacher, H. Schmalz, A. H. E. Müller, *Nature*, **2013**, 503, 247.

[171] Z. Li, N. S. Lee, K. L. Wooley, *J. Am. Chem. Soc.* **2011**, 133, 5, 1228.

[172] A. Walther, C. Barner-Kowollik, A. H. E. Müller, *Langmuir*, **2010**, 26, 14, 12237.

[173] Y. Sun, B. Xu, X. Tao, X. Li, S. Lin, *Mater. Chem. Front.* **2022**, 6, 908.

[174] S. Jang, K. Kim, J. Jeon, D. Kang, B. H. Sohn, *Soft Matter* **2017**, 13, 6756.

[175] S. Chae, S. Lee, K. Kim, S. W. Jang, B. H. Sohn, *Chem. Commun.* **2016**, 52, 6475.

[176] K. Kim, S. Jang, J. Jeon, D. Kang, B. H. Sohn, *Langmuir*, **2018**, 34, 15, 4634.

[177] K. Liu, Z. Nie, N. Zhao, W. Li, M. Rubinstein, E. Kumacheva, *Science*, **2010**, 329, 5988, 197.

[178] X. Zhang, L. Lv, G. Wu, D. Yang, A. Dong, *Chem. Sci.* **2018**, 9, 3986.

[179] J. Kim, M. R. Jones, Z. Ou, Q. Chen, *ACS Nano*, **2016**, 10, 11, 9801.

[180] Z. Zhuang, T. Jiang, J. Lin, L. Gao, C. Yang, L. Wang, C. Cai, *Angew. Chem.* **2016**, 128, 12710.

[181] X. Ma, Y. Zhou, L. Zhang, J. Lin, X. Tian, *Nanoscale* **2018**, 10, 16873.

[182] Y. Lu, L. Gao, J. Lin, L. Wang, L. Zhang, C. Cai, *Polym. Chem.* **2019**, 10, 3461.

[183] S. Stuij, J. Rouwhorst, H. Jonas, N. Ruffino, Z. Gong, S. Sacanna, P. Bolhuis, P. Schall, *Phys. Rev. Lett.* **2021**, 127, 108001.

[184] H. Wang, L. Chen, X. Shen, L. Zhu, J. He, H. Chen, *Angew. Chem. Int. Ed.* **2012**, 51, 8021.

[185] N. G. Pavlopoulos, J. T. Dubose, E. D. Hartnett, K. Char, J. Pyun, *ACS Macro Lett.* **2016**, 5, 8, 950.

[186] X. Ma, M. Gu, L. Zhang, J. Lin, X. Tian, *ACS Nano*, **2019**, 13, 2, 1968.

[187] S. Lee, S. Jang, K. Kim, J. Jeon, S. S. Kim, B. H. Sohn, *Chem. Commun.* **2016**, 52, 9430.

[188] H. R. Vutukuri, A. F. Demirörs, B. Peng, P. D. J. van Oostrum, A. Imhof, A. van Blaaderen, *Angew. Chem. Int. Ed.* **2012**, 51, 11249.

[189] S. Pawłowska, T. A. Kowalewski, F. Pierini, *Soft Matter* **2018**, 14, 8421.

[190] S. G. Stuij, H. J. Jonas, Z. Gong, S. Sacanna, T. E. Kodger, P. G. Bolhuis, P. Schall, *Soft Matter*, **2021**, 17, 8291.

[191] S. L. Biswal, A. P. Gast, *Phys. Rev. E.* **2003**, 68, 021402.

[192] A. McMullen, M. Holmes-Cerfon, F. Sciortino, A. Y. Grosberg, J. Brujic, *Phys. Rev. Lett.* **2018**, 121, 138002.

[193] X. Zheng, M. Liu, M. He, D. J. Pine, M. Weck, *Angew. Chem. Int. Ed.* **2017**, 56, 5507.

[194] L. J. Hill, N. Pinna, K. Char, J. Pyun, *Prog. Polym. Sci.* **2015,** 40, 85.

[195] Y. Zhang, T. Guan, G. Han, T. Guo, W. Zhang, *Macromolecules*, **2019**, 52, 2, 718.

[196] J. S. Graham, B. R. McCullough, H. Kang, W. A. Elam, W. Cao, E. M. de La Cruz, *PLoS One* **2014**, 9, 4, e94766.

[197] G. Odian, *Principles of Polymerization*, 4th ed., Wiley-Interscience, **2004**.

[198] P. C. Hiemenz, T. P. Lodge, *Polymer Chemistry*, 2nd ed., CRC Press, **2007**.

[199] S. G. Stuij, A. Biebricher, Z. Gong, S. Sacanna, E. Peterman, I. Heller, P. Schall, *Phys. Rev. Mater.* **2022**, 6, 035603.

[200] J. Xue, T. Wu, Y. Dai, Y. Xia, *Chem. Rev.* **2019**, 119, 8, 5298.

[201] Q. Huang, Y. Zhu, *ACS Appl. Mater. Interfaces*, **2021**, 13, 51, 60736.

[202] W. Li, H. Zhang, S. Shi, J. Xu, X. Qin, Q. He, K. Yang, W. Dai, G. Liu, Q. Zhou, H. Yu, S. R. P. Silva, M. Fahlman, *J. Mater. Chem. C*, **2020**, 8, 4636.

[203] T. Sannicolo, M. Lagrange, A. Cabos, C. Celle, J. P. Simonato, D. Bellet, *Small*, **2016**, 12, 44, 6052.

[204] J. L. Wang, M. Hassan, J. W. Liu, S. H. Yu, *Adv. Mater.* **2018**, 30, 1803430.

[205] D. J. Lunn, O. E. C. Gould, G. R. Whittell, D. P. Armstrong, K. P. Mineart, M. A. Winnik, R. J. Spontak, P. G. Pringle, I. Manners, *Nat Commun* **2016**, 7, 12371.

[206] A. Aggarwal, S. Naskar, A. K. Sahoo, S. Mogurampelly, A. Garai, P. K. Maiti, *Curr. Opin. Struct. Biol*, **2020**, 64, 42.

[207] H. Isambert, P. Venier, A. C. Maggs, A. Fattoum, R. Kassab, D. Pantaloni, M. F. Carlier, *J. Biol. Chem.* **1995**, 270, 19, 11437.

[208] J. Baschnagel, H. Meyer, J. Wittmer, I. Kulić, H. Mohrbach, F. Ziebert, G. M. Nam, N. K. Lee, A. Johner, *Polymers*, **2016**, 8, 8, 286.

[209] Z. Yin, Y. Wang, C. Song, L. Zheng, N. Ma, X. Liu, S. Li, L. Lin, M. Li, Y. Xu, W. Li, G. Hu, Z. Fang, D. Ma, *J. Am. Chem. Soc.* **2018**, 140, 3, 864.

[210] Q. Su, M. T. Zhou, M. Z. Zhou, Q. Sun, T. Ai, Y. Su, *Front Chem* **2020**, 8, 836.

[211] X. Li, J. Iocozzia, Y. Chen, S. Zhao, X. Cui, W. Wang, H. Yu, S. Lin, Z. Lin, *Angew. Chem. Int. Ed.* **2018**, 57, 2046.

[212] C. Yi, Y. Yang, B. Liu, J. He, Z. Nie, *Chem. Soc. Rev.* **2020**, 49, 465.

[213] V. F. Puntes, K. M. Krishnan, P. Alivisatos, *Appl Phys Lett* **2001**, 78, 2187.

[214] J. Saiz-Poseu, J. Mancebo-Aracil, F. Nador, F. Busque, D. Ruiz-Molina, *Angew. Chem. Int. Ed.* **2019**, 58, 696.

[215] Q. Lyu, N. Hsueh, C. L. L. Chai, *ACS Biomater. Sci. Eng.* **2019**, 5, 6, 2708.

[216] M. Poutanen, G. Guidetti, T. I. Gröschel, O. v. Borisov, S. Vignolini, O. Ikkala, A. H. Gröschel, *ACS Nano*, **2018**, 12, 4, 3149.

국문 초록

고분자의 나노 크기 유사체로서의 이중블록 공중합체 마이셀 초콜로이드 사슬

이 경 현
화학부 고분자화학 전공
서울대학교 대학원

나노 및 마이크로 크기의 콜로이드 입자는 입자 간 상호작용을 통해 자발적으로 조립하여 결정, 사슬, 클러스터와 같은 정렬된 초구조를 형성한다. 이러한 콜로이드 초구조는 개별 입자에서는 관찰되지 않는 복잡한 구조와 집합적 특성으로 인해 새로운 나노 소재로서 활발히 연구되고 있다. 특히 콜로이드 입자 사이에 양 방향 인력과 그에 수직한 반발력이 작용하는 경우 선형의 초콜로이드 사슬을 조립할 수 있다. 예를 들어, 자기 및 정전기 쌍극자를 가진 콜로이드 입자들은 쌍극자 간 상호작용을 통해 초콜로이드 사슬로 조립되며 이 과정에서 리간드 사이의 반발력에 의해 수직한 응집은 억제된다.

초콜로이드 사슬은 구성 입자와는 구분되는 집합적, 구조적 특성으로 다양하게 응용될 수 있다. 입자 간 상호작용을 통해 플라즈몬 및 자기 커플링 특성을 보이는 초콜로이드 사슬은 전기적, 자기적 응용에 활용될 수 있으며, 초콜로이드 사슬의 극도로 비등방적인 선형 구조는 일차원 광결정, 유변학적 유체, 콜로이드 모터 등에 응용 가능한 광학적, 기계적 특성을 부여한다.

콜로이드 입자 표면에 화학적, 물리적으로 구분되는 영역인 패치를 도입하는 방법 또한 입자의 선형 조립을 위한 효과적인 전략이다. 양 방향 조립을 위해서는 각 입자마다 두 개의 패치가 요구되며 이러한 패치는 수소 결합, 호스트-게스트 상호작용, 소수성 상호작용 등 다양한 화학적 상호작용을 통해 입자 사이의 인력을 유발한다. 특히, 블록 공중합체 마이셀 표면에 코로나의 미세상 분리를 통해 패치를 도입하여 초콜로이드 사슬로 조립할 수 있다.

콜로이드 단량체가 반복되어 선형으로 조립된 초콜로이드 사슬은 전통적인 고분자의 나노크기 유사체로 비유할 수 있으며, 이러한 관점에서 초콜로이드 사슬의 거동을 고분자의 전통적인 이론으로 설명할 수 있다. 초콜로이드 사슬의 조립 과정의 경우 고분자 중합 이론인 단계 및 연쇄 중합 메커니즘을 통해 설명한 연구들이 보고되었다. 또한 초콜로이드 사슬의 크기를 경로 길이 (contour length), 양 끝 간 거리(end-to-end distance), 반경(radius of gyration)과 같은 고분자의 크기 척도로 정의할 수 있으며 이를 기반으로 초콜로이드

사슬의 유연성과 형태를 freely jointed chain, worm-like chain 모델과 같은 고분자 사슬 모델로 설명할 수 있음이 보고되었다. 이러한 고분자와의 유사성에 기반한 분석은 요구되는 특성과 구조를 가지는 초콜로이드 사슬의 조립을 위한 기초 연구로서 중요한 의미를 가진다. 나아가 전통적인 고분자에 적용된 다양한 가공 및 기능화 방법을 적용하여 초콜로이드 사슬의 응용 영역을 넓힐 수 있다.

본 학위논문에서는 전통적인 고분자의 유사체로서의 PS-*b*-P4VP 이중블록 공중합체 마이셀 초콜로이드 사슬의 거동을 주로 다룬다. 구형의 PS-*b*-P4VP 마이셀을 콜로이드 단량체인 패치 마이셀로 변화시키고 패치 사이의 소수성 상호작용을 통해 조립하여 초콜로이드 사슬을 조립하였다. 본 논문은 초콜로이드 사슬의 형성 과정과 물리적 특성을 이해하고 가공 및 기능화를 통해 응용 전략을 제시하는 것을 목적으로 한다. 제 2 장에서는 초콜로이드 사슬의 조립 과정을 논의한다. 수평균 중합도의 선형적 증가와 2 로 근접하는 다분산지수의 변화로부터 패치 마이셀이 단계 중합(step-growth polymerization)의 메커니즘을 따라 초콜로이드 사슬로 중합됨을 확인하였다. 조립 메커니즘에 대한 이해를 바탕으로 농도를 조절하여 중합 속도를 조절하고 고리 형태 초콜로이드 사슬을 중합하였다. 패치 마이셀이 패치의 용해도 감소로 인해 중합되므로 물 함량 및 패치 크기가 증가함에 따라 빠르게 중합됨을 확인하였다. 제 3 장에서는 초콜로이드 사슬의 유연성과 형태를 분석하였다. 초콜로이드 사슬의

지속 길이(persistence length)를 평가하여 초콜로이드 사슬이 세미유연성(semi-flexible)임을 확인하였으며, 전통적인 고분자와 마찬가지로 초콜로이드 사슬의 형태가 worm-like chain 모델로 설명됨을 확인하였다. 세미유연성 초콜로이드 사슬을 코팅하여 다공성 자기 지지 필름을 제조하였다. 제 4 장에서는 초콜로이드 사슬의 단량체로서 코발트 나노입자를 포함한 PS-*b*-P4VP 마이셀을 보고하였다. 코발트 나노입자를 PS-*b*-P4VP 로 감싸 코발트 나노입자-P4VP 쉘-PS 코로나로 구성된 구형 마이셀을 유도하였다. P4VP 쉘을 가교한 후 PS 코로나의 상분리를 유도하여 표면에 패치를 유도하였다. 최종적으로 패치 마이셀 용액에 물을 첨가하여 초콜로이드 사슬을 조립하였다. 이 과정에서 침전을 막기 위해 P4VP 쉘을 CH_3I 과 반응시켜 추가적인 반발력을 도입하였다.

주요어: 블록 공중합체 마이셀, 자기 조립, 초콜로이드 사슬, 단계 중합, 세미유연성 사슬, Worm-like chain 모델, 자기 지지 필름, 코발트 나노입자.

학 번: 2017-29824.